

Dynamics of the NGC 4636 Globular Cluster System [★]

An extremely dark matter dominated galaxy?

Y. Schuberth^{1,2}, T. Richtler², B. Dirsch², M. Hilker¹, S. S. Larsen³, M. Kissler-Patig³, and U. Mebold¹

¹ Argelander-Institut für Astronomie **, Universität Bonn, Auf dem Hügel 71, D-53121 Bonn, Germany

² Universidad de Concepción, Departamento de Física, Casilla 160-C, Concepción, Chile

³ European Southern Observatory, Karl-Schwarzschild-Str. 2, D-85748 Garching, Germany

Received March –, 2005; accepted April 6, 2006

ABSTRACT

Context. We present the first dynamical study of the globular cluster system of NGC 4636. It is the southernmost giant elliptical galaxy of the Virgo cluster, and is claimed to be extremely dark matter dominated, according to X-ray observations.

Aims. Globular clusters are used as dynamical tracers to investigate, by stellar dynamical means, the dark matter content of this galaxy.

Methods. Several hundred medium resolution spectra were acquired at the VLT with FORS 2/MXU. We obtained velocities for 174 globular clusters in the radial range $0'.90 < R < 15'.5$, or $0.5 - 9 R_e$ in units of effective radius. Assuming a distance of 15 Mpc, the clusters are found at projected galactocentric distances in the range 4 to 70 kpc, the overwhelming majority within 30 kpc. The measured line-of-sight velocity dispersions are compared to Jeans-models.

Results. We find some indication for a rotation of the red (metal-rich) clusters about the minor axis. Out to a radius of 30 kpc, we find a roughly constant projected velocity dispersion for the blue clusters of $\sigma \approx 200 \text{ km s}^{-1}$. The red clusters are found to have a distinctly different behavior: at a radius of about $3'$, the velocity dispersion drops by $\sim 50 \text{ km s}^{-1}$ to about 170 km s^{-1} which then remains constant out to a radius of $7'$. The cause might be the steepening of the number density profile at $\sim 3'$ observed for the red clusters. Using only the blue clusters as dynamical tracers, we perform Jeans-analyses for different assumptions of the orbital anisotropy. Enforcing the model dark halos to be of the NFW type we determine their structural parameters. Depending on the anisotropy and the adopted M/L-values, we find that the dark matter fraction within one effective radius can vary between 20% and 50% with most a probable range between 20% and 30%. A main source of uncertainty is the ambiguity of the velocity dispersion in the outermost bin. A comparison with cosmological N-body simulations reveals no striking disagreement.

Conclusions. Although the dark halo mass still cannot be strongly constrained, NGC 4636 does not seem to be extremely dark matter dominated. The derived circular velocities are also consistent with Modified Newtonian Dynamics.

Key words. Galaxies: elliptical and lenticular, cD – Galaxies: star clusters – Galaxies: halos – Galaxies: kinematics and dynamics – Galaxies: individual NGC 4636

1. Introduction

1.1. Work on NGC 4636

NGC 4636 is the southernmost bright elliptical in the Virgo cluster of galaxies. It is located 10° south of M 87, within the Virgo Southern Extension. Surface brightness fluctuation (SBF) measurements yield a distance of 15 Mpc (Tonry et al. 2001), which we adopt throughout this paper. This value, however, has to be considered as a lower limit, since mea-

surements based on the globular cluster luminosity function (GCLF) presented by Kissler et al. (1994) and Dirsch et al. (2005) point towards a larger distance of more than 17 Mpc. Table 1 summarizes the basic properties of NGC 4636.

Although NGC 4636, being an elliptical galaxy, predominantly consists of an old stellar population, there are some weak indications of an intermediate age population: firstly, it is a supernova Ia host galaxy (SN 1939a: Zwicky 1939, Giclas 1939), and there are theoretical considerations that this type of supernova originates in intermediate age populations rather than in very old ones (Yungelson et al. 1995 and Yoshii et al. 1996). Secondly, far infrared observations by Temi et al. (2003) hint at a recent merger which supplied NGC 4636 with extra dust.

In the 1970s NGC 4636 was the target of several H I-observations. Despite some claims of an extended H I-emission

Send offprint requests to: ylva@astro.uni-bonn.de

* Based on observations collected at the European Southern Observatory, Cerro Paranal, Chile; ESO program 69.B-0366.

** Founded by merging of the Institut für Astrophysik und Extraterrestrische Forschung, the Sternwarte, and the Radioastronomisches Institut der Universität Bonn.

(Knapp et al. 1978, Bottinelli & Gouguenheim 1978), the deepest observations performed by Krishna Kumar & Thonnard (1983), yielded an upper limit of only $11.5 \times 10^7 M_{\odot}$ to the total H I mass of NGC 4636.

Because of its high X-ray luminosity, NGC 4636 has been studied extensively in this frequency range and these observations have also been used to infer its dark matter content and distribution.

Forman et al. (1985) analyzed Einstein X-ray data from a large sample of early type galaxies. For NGC 4636 they found extended emission (out to a radius of $R_{\max} = 44$ kpc) and derived an X-ray luminosity of $L_X = 1.78 \pm 0.10 \times 10^{41}$ ergs s^{-1} . They quote a mass-to-light ratio $M_{\text{total}}/L_B = 87$ for R_{\max} , the second largest value in their sample.

Matsushita et al. (1998), using ASCA, found very extended X-ray emission around NGC 4636 out to $60'$. This corresponds to a radius of almost 300 kpc in a distance of 15 Mpc. The authors suggest that the gravitational halo of NGC 4636 itself terminates in the region between 10 and 30 kpc. They observe an increase in mass beyond 30 kpc forming a halo-in-halo structure, whose size is comparable to that of a galaxy group.

Jones et al. (2002) used the Chandra X-Ray Observatory Advanced CCD Imaging Spectrometer (ACIS) to study the X-ray halo of NGC 4636 with a spatial resolution of ~ 50 pc. The observed X-ray features are so far unique: the images show symmetric, arm-like structures which surround a bright central region. These structures extend ~ 8 kpc from the galaxy center. The leading edges of these arms show changes in brightness by a factor of two on scales of just a few arcseconds. While these sharp fronts might be suggestive of a merger, the authors favor a nuclear outburst as the source of the observed morphology. They interpret the arms as the projected edges of paraboloidal

shock fronts expanding from the nucleus. Jones et al. speculate that the unusually high X-ray luminosity of NGC 4636 might be due to the advanced state of the cooling that brought on the outburst and may be further enhanced by the shocks. When the gas halo returns to hydrostatic equilibrium, the X-ray luminosity could decline by an order of magnitude or more.

Loewenstein & Mushotzky (2003) used the Chandra X-Ray Observatory to measure the hot interstellar medium temperature profile of NGC 4636. Assuming hydrostatic equilibrium, they determined the total enclosed mass profile for the radial range $0.7 < r < 35$ kpc. These authors come to the conclusion that dark matter constitutes a large fraction (between 50% and 80%) of the total mass even inside the effective radius.

Given all these peculiarities, it is of great interest to use globular clusters as dynamical tracers in order to evaluate the dark matter content of NGC 4636. This work continues our programme on the dynamics of globular cluster systems around early-type galaxies. Previous papers on NGC 1399, the central galaxy of the Fornax cluster are Richtler et al. (2004) and Dirsch et al. (2003).

1.2. The NGC 4636 Globular Cluster System

The globular cluster system of NGC 4636 has been the target of three photometric studies. Hanes (1977) used photographic plates to assess the number and the luminosity of the GCs. He derived a specific frequency (i.e. the number of GCs normalized to the host galaxy's luminosity (Harris & van den Bergh 1981) of $S_N = 9$, which is unusually high for a quite isolated elliptical galaxy. Most field ellipticals have S_N values between 3 and 4. The first CCD-study was performed by Kissler et al. (1994) who observed a field of 7.5×7.5 centered on NGC 4636 in one band (Cousins V, limiting magnitude of 24.25). They estimated the total number of GCs to 3600 ± 200 , which corresponds to $S_N = 7.5 \pm 2.0$, hence supporting the unusually high number of GCs.

The full extent of the GCS together with color information only became apparent in the recent study of Dirsch et al. (2005). They used the MOSAIC camera at the 4-m telescope at the Cerro Tololo Interamerican Observatory (CTIO). The bands were Kron-Cousins R and Washington C. The final images have a field-of-view of 34.7×34.7 . The color distribution of the GCs shows the familiar bimodal shape. The color of the minimum of the inner sample (C-R=1.55) was chosen to divide red (metal-rich) from blue (metal-poor) clusters, frequently interpreted as two different sub-populations (e.g. Ashman & Zepf 1998, Kundu & Whitmore 2001, Larsen et al. 2001). For the total number of globular clusters Dirsch et al. derived 3700 ± 200 , which agrees well with the previous measurement. The specific frequency S_N ranges between 5.8 ± 1.2 and 8.9 ± 1.2 , for the GCLF and SBF distance, respectively. An interesting feature shows up in the radial distribution of the clusters: While the (projected) radial number density distribution of the blue clusters can be described by one power-law ($n(r) \propto r^\alpha$) within $1' - 8'$, the density distribution of the red clusters changes the exponent within this radial interval. At a radial distance of $7' (9')$ for the red (blue) clusters, the power-law exponent drops

Table 1. NGC 4636 basic data compiled from the literature (1) NED, (2) Tonry et al. (2001), (3) this work, (4) R3C, (5) Dirsch et al. (2005), (6) Bender et al. (1994), (7) Idiart et al. (2003), (8) Forman et al. (1985), (9) Loewenstein et al. (2001).

Other names	UGC 07878, VCC 1939	
Position (J2000)	$12^{\text{h}} 42^{\text{m}} 50^{\text{s}} +02^{\circ} 41' 17''$	(1)
Galactic coordinates	$l = 297.75^{\circ} b = 65.47^{\circ}$	
SBF distance modulus	$(m - M) = 30.83 \pm 0.13$	(2)
Distance	$D = 15$ Mpc	
Scale	$1'' = 73$ pc $1' = 4.4$ kpc	
GCLF distance modulus	$(m - M) = 31.24 \pm 0.17$	(5)
Heliocentric velocity	$v_{\text{helio}} = 906 \pm 7$ km s^{-1}	(3)
Hubble type	E0+	(4)
Ellipticity	$\epsilon = 0.15$	(6)
Position angle	$PA = 145^{\circ}$	(5)
Effective radius	$R_e = 101''$ ($= 7.5$ kpc)	(7)
Blue magnitude	$B_T = 10.43$	(4)
Total apparent magnitude	$T1 = 8.70 \pm 0.05$	(5)
Metallicity	$[Fe/H] = -0.01$ dex	(7)
X-ray luminosity	$L_X = 1.78 \pm 0.10 \times 10^{41}$ ergs/s	(8)
Nuclear X-ray emission	$\leq 2.7 \times 10^{38}$ ergs/s	(9)

to about -5 (cf. Table 3 in Dirsch et al. 2005) Such behavior has not been observed in any GCS before. This abrupt decrease in number density might mark the limit of the GCS and possibly that of the galaxy itself. The photometric data by Dirsch et al. forms the basis of the candidate selection for our spectroscopic observations described in the following section.

2. Observations

The observations were carried out during four nights (May 7–10 2002) at the European Southern Observatory (ESO) Very Large Telescope (VLT) facility at Cerro Paranal, Chile. The VLT Unit Telescope 4 was used with the FORS2 (FOcal Reducer/low dispersion Spectrograph) instrument equipped with the Mask EXchange Unit (MXU). The standard resolution collimator used for this program provided a field-of-view of $6'.8 \times 6'.8$. The detector system consisted of two 4096×2048 red optimized CCDs with a pixel size of $15 \mu\text{m}$. For our observations the chips were read out using a 2×2 binning. The grism 600B gave a spectral resolution of about 3 \AA . The spectral coverage was dependent on the slit position on the mask. In most cases, the usable coverage was about 2000 \AA with limits on the red side varying between 5500 and 6500 \AA . We exposed 13 spectroscopic masks, the preparation of which is described in the next section. Flat fielding was done with internal flat lamps. A Hg-Cd-He lamp was used for wavelength calibration. The observations are summarized in Table 2.

2.1. Mask Preparation

Pre-images of the 13 pointings in 7 fields (see Fig. 1) were obtained in service mode in October 2000. Each pointing was observed in Cousins V and I filters for 30 seconds. The GC candidate selection was based upon the photometric work presented in Dirsch et al. (2005). Cluster candidates had to fulfill the following criteria: they had to be brighter than 22.7 in R and the allowed color range was $0.9 < C-R < 2.1$. Further, the candidates should exhibit a star-like appearance on the pre-images to distinguish them from background galaxies. The ESO FORS Instrumental Mask Simulator (FIMS) software was then used to select the positions, widths and lengths of the slits. A slit width of $1''$ was chosen according to the sub-arcsecond seeing conditions on Paranal. To maximize the number of GC spectra obtained per mask, we chose to observe our targets and sky positions through separate slits of $2''$ length. Obviously, the quality of the sky subtraction then depends on the accuracy of the wavelength calibration. As it will be shown, it turned out to be satisfactory to obtain radial velocities with the desired accuracy. After positioning the slits for the selected GC candidates, the remaining space on the masks (especially in the outer fields) was used to include additional objects. Thus, also background galaxies and point sources not matching the above-mentioned criteria were observed.

2.2. The Data Set

The MXU-observations of our thirteen fields have exposure times in the range of 3600 to 7200 seconds (see Table 2 for a

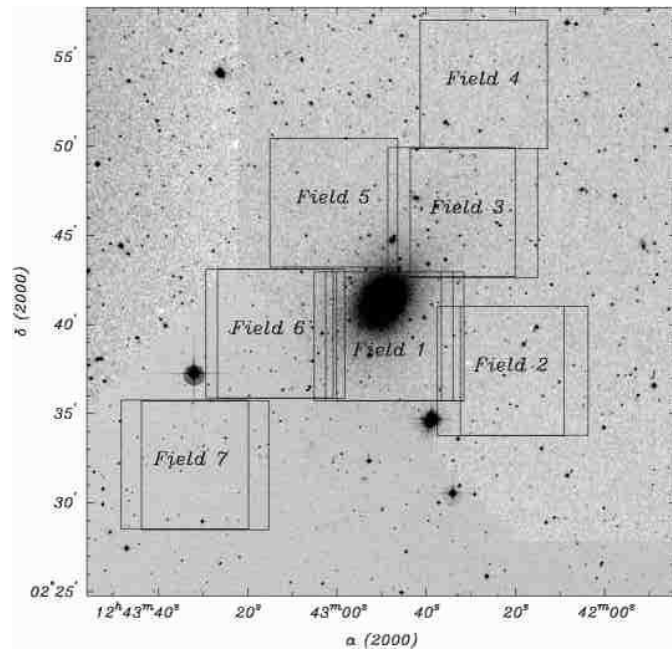


Fig. 1. Positions of the fields overlaid on a $33' \times 33'$ DSS image centered on NGC 4636. For each mask the entire FORS 2 $6'.8 \times 6'.8$ field-of-view is shown. Note that the slit positions are confined to the central $4'.3 \times 6'.8$ region of each pointing.

summary of the observations). To minimize the effects from cosmic ray hits, the observation of each mask was divided into two exposures - with the exception of Field 1.1 for which three science images were obtained. In addition to the spectroscopic observations, calibration measurements, i.e. bias, flat fields and wavelength calibration exposures were obtained during day time.

3. Data Reduction

The following section summarizes the reduction steps performed to obtain the final sky-subtracted spectra. Most of the data reduction was done within the IRAF-environment¹.

3.1. Basic Reduction

The merging of the two CCD-frames was done with *fsmosaic* which is available as a part of the ESO-FIMS software. The dimension of the combined images is 2050×2076 pixels. For cosmic ray removal, the task *bclean* from the *Starlink Figaro*-package was found to perform best. Biasing and flat-fielding was done in the standard way. Since the aim of this study is the measurement of radial velocities rather than the measurement of line strengths, we did not apply any response function fitting or flux calibration. To obtain one-dimensional spectra (aperture definition, tracing, and extraction) the IRAF task *apall* from the

¹ IRAF (Image Reduction and Analysis Facility) is distributed by the National Optical Astronomy Observatories, which are operated by the Association of Universities for Research in Astronomy, Inc., under cooperative agreement with the National Science Foundation. (<http://iraf.noao.edu/>)

Field	Center Position		Exp. Time (sec)	Seeing	# Slits		# GCs	Night	UT (start)
	(J2000)				total	objects			
1.1	12:42:48.2	02:39:21.0	7200	1''1	111	79	39	2002-05-07	23:27
1.2	12:42:45.8	02:39:24.2	4500	0''9	98	61	47	2002-05-07	01:49
1.3	12:42:50.8	02:39:21.3	5400	1''2	106	65	26	2002-05-07	03:17
2.1	12:42:17.8	02:37:27.9	3600	1''0	101	51	3	2002-05-07	05:11
2.2	12:42:23.0	02:37:27.6	3600	1''0	99	48	2	2002-05-08	23:32
3.1	12:42:34.2	02:46:22.4	3600	0''8	113	77	26	2002-05-08	01:21
3.2	12:42:28.9	02:46:20.7	3600	1''1	113	54	14	2002-05-08	02:31
4.1	12:42:27.1	02:53:27.4	3600	1''3	98	44	2	2002-05-10	23:37
5.1	12:43:00.6	02:46:50.3	3600	0''9	105	17	59	2002-05-08	03:43
6.1	12:43:15.0	02:39:33.7	3600	1''2	107	53	8	2002-05-10	01:04
6.2	12:43:12.6	02:39:32.0	3600	0''9	110	55	16	2002-05-09	00:18
7.1	12:43:33.9	02:32:12.1	3600	0''9	109	52	0	2002-05-09	01:31
7.2	12:43:29.3	02:32:09.7	3600	0''8	113	59	2	2002-05-09	02:44

Table 2. Summary of observations (ESO program ID 69.B-0366(B)). The seeing values were determined from the acquisition images taken just before the MXU exposures.

apextract package was used. Once the aperture positions were defined on the science images, they were checked and - where necessary - adjusted on the flatfield divided exposures. For the 2'' long slits used for most sources, an aperture size of 4 pixels (= 1'') was found to yield the best results.

3.2. Wavelength Calibration and Sky Subtraction

The one-dimensional arc lamp spectra were calibrated using the interactive task *identify* from the *noao.onedspec* package. The dispersion/wavelength solution was approximated by a seventh-order Chebyshev polynomial. The residuals of this fit were inspected for outliers, and if necessary the deviant data points were excluded from the fit in the next step. The RMS errors of the final fits were about 0.04 Å. As described above, sky spectra were measured through separate slits. In order to perform the sky subtraction for a given GC-spectrum, two or three adjacent (within 18'') of these sky spectra were combined. This combined spectrum was then subtracted using the *skytweak* task.

4. Measurement of radial velocities

The IRAF task *fxcor* from the *noao.rv* package performs a Fourier cross-correlation on the input object and template spectra. This program is based upon the technique developed by Tonry & Davis (1979). For the cross-correlation, a template with a high S/N and a spectrum similar to that of a globular cluster is required. NGC 4636 itself, however is not suitable due to its high velocity dispersion of about 200 km s⁻¹. Therefore, the velocities were measured using a spectrum (S/N ~ 30) of NGC 1396 as template. This spectrum was obtained in Dec. 2000, during observations of the NGC 1399 GCS, using the same FORS2 instrumental setup and has already been used as template for investigating the kinematics of the NGC 1399 GCS (Dirsch et al. 2004). NGC 1396 is a dwarf elliptical galaxy close to NGC 1399, and its spectrum resembles that of a metal-rich globular cluster. Its velocity dispersion is only 65 ± 6 km s⁻¹

(Wegner et al. 2004). We adopted a heliocentric radial velocity of 815 ± 8 km s⁻¹ (Dirsch et al. 2004). The velocities obtained with this template were checked with a second template spectrum obtained during our observations (object 1.3:56), a bright star whose observed velocity was found to be -682 km s⁻¹ with respect to the galaxy template. The velocities measured with the two different templates agree very well. Since the *fxcor* uncertainty estimates were smaller for the galaxy template, only these velocities are used for the subsequent analysis. The accuracy of the velocity determination depends on the shape of the spectrum, and the wavelength range for which the cross-correlation is performed. A range of 4700 < λ < 5500 Å was found to be an appropriate choice in most cases. The upper limit was chosen to avoid the night sky emission lines found around the strong [OI] 5577 Å feature. In some spectra however, the relatively weak Nitrogen line at 5199 Å left substantial residuals: where this was the case, the wavelength interval was adjusted accordingly. For the velocities of the NGC 4636 GCS, we applied a heliocentric correction of $v_{\text{hc}} = -18 \text{ km s}^{-1}$; the correction for the NGC 1396 spectrum is $v_{\text{hc}} = -10 \text{ km s}^{-1}$. The uncertainty for the velocities is estimated using:

$$\Delta v = \sqrt{\Delta v_{\text{fxcor}}^2 + \Delta v_{\text{template}}^2},$$

where Δv_{fxcor} is the velocity uncertainty output by *fxcor*, and $\Delta v_{\text{template}}$ is the velocity uncertainty of the template spectrum.

4.1. Zero Point Shifts

Since the wavelength calibration exposures for each mask were obtained during the day following the observation, the mask was moved into the focal plane again. The finite positioning accuracy of the MXU, and shifts due to instrument flexure under gravity - all calibration exposures are obtained with the telescope pointing at the zenith - result in an offset between the science and the calibration images. This offset manifests itself as a zero point shift in the observed wavelength of the strong telluric [OI] 5577 Å emission line. The zero point shifts in our

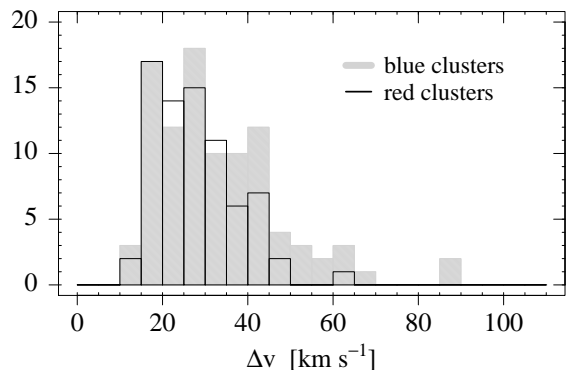


Fig. 2. Histogram of the velocity uncertainties calculated by the *fxcor*-task. The grey histogram shows the values for the blue clusters, the black histogram shows the same for the red clusters.

data set were found to vary with the position of the slit along the y -axis of the mask. To quantify this effect, the wavelength of the 5577\AA line was measured in all spectra for a given mask. A linear function was fit to the data and provided a velocity correction for every aperture. These corrections have values in the range $-25\text{ km s}^{-1} \leq \Delta v_{\text{MXU}} \leq 25\text{ km s}^{-1}$.

To measure the systemic velocity of NGC 4636, we used the nine spectra of NGC 4636 from mask 1_1, and found a heliocentric velocity of $906 \pm 7\text{ km s}^{-1}$. In the NASA/IPAC Extragalactic Database (NED)² one finds seven optical velocity measurements with uncertainty estimates. The mean is $917 \pm 31\text{ km s}^{-1}$. Hence, our velocity agrees very well with previous measurements.

4.2. Velocity Uncertainties

For the GCs, no trend is visible for the metal poor (blue) and the metal rich (red) subpopulations: both have very similar error distributions (see Fig. 2). Figure 3 shows the velocity uncertainties as a function of apparent R-magnitude. As expected, the measurements of fainter objects tend to have larger uncertainties. The uncertainties returned by the *fxcor* task are computed according to the formulae given by Tonry and Davis (1979). To check whether these uncertainties are a realistic error estimate, we compared the velocities of those 40 objects for which we had two spectra since they were present on two masks. The mean difference for the velocity measurements was found to be very similar to the mean of the uncertainties given by *fxcor*. Hence, the *fxcor* uncertainties can be considered a good error estimate. The velocities determined for the GCs are listed in appendix A which is available in electronic form.

5. Properties of the Globular Cluster Sample

For every object with a velocity measurement, the color and magnitude information was extracted from the photometry-

² The NASA/IPAC Extragalactic Database (NED) is operated by the Jet Propulsion Laboratory, California Institute of Technology, under contract with the National Aeronautics and Space Administration.

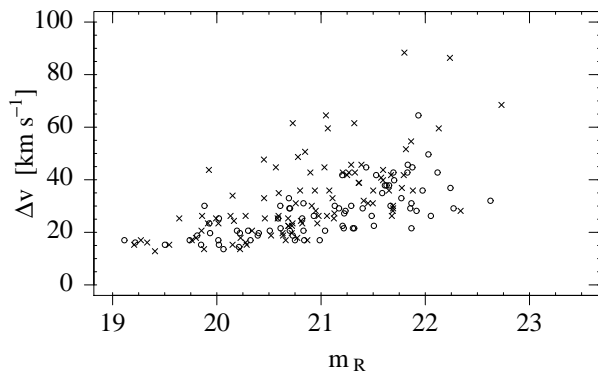


Fig. 3. Velocity uncertainties versus R-magnitude for the globular clusters (crosses: blue clusters; open circles: red clusters).

database from Dirsch et al. (2005) via coordinate matching. The coordinates, velocities, C – R -colors and apparent R magnitudes of these objects are listed in appendix A. For two clusters, neither color nor magnitude information exists, since they happened to be located near a bad row of the MOSAIC-CCD.

5.1. Defining the Sample

The first step was to divide our data set into GCs and foreground stars. A compelling distinction between stars and globular clusters would be given if the GCs could be resolved on the acquisition images. However, only very few, about three, of our clusters are marginally resolved. Guided by Fig. 4 which shows the distribution of velocity versus color for all measured objects, a lower limit of 350 km s^{-1} for the radial velocity of the GCs was chosen. However, one has to be aware that there might be a velocity domain where this identification is doubtful. Given that the Galactic rotation vector towards the position of NGC 4636 is -78 km s^{-1} , one cannot exclude that foreground stars have heliocentric velocities of up to 400 km s^{-1} . Neither can one rule out the presence of GCs with radial velocities of more than 500 km s^{-1} relative to NGC 4636.

The range in velocities occupied by foreground stars and globular clusters is $-248 \leq v \leq 313\text{ km s}^{-1}$ and $392 \leq v \leq 1441\text{ km s}^{-1}$, respectively. The data set comprises 174 globular clusters and 175 foreground stars. The basic properties of the GC sample are listed in Table 3. The so-defined GCs appear in Fig. 5 which shows their distribution around NGC 4636. The inner region is well sampled, but due to the sharp drop-off at $\sim 7'$ only a handful of clusters is located outside this radius.

5.2. Color and Luminosity Distribution

For any further investigation, it is important that the color distribution of the GCs with measured radial velocities resembles that of the entire cluster system. Indeed, the bimodality of the color distribution found in the photometric study by Dirsch et al. (2005) is clearly visible in our much smaller sample (see Fig. 6). For consistency, the same dividing color of $C - R = 1.55$ was used. Thus, we find 97 blue and 75 red

	all	blue	red
number of GCs	174	97	75
mean velocity [km s^{-1}]	904	911	887
min. velocity [km s^{-1}]	392	514	392
max. velocity [km s^{-1}]	1441	1441	1273
mean vel. uncertainty [km s^{-1}]	31	33	28
velocity dispersion [$\sigma(R) \text{ km s}^{-1}$]	203 ± 11	202 ± 15	199 ± 17
color range C-R		0.85 - 1.55	1.55 - 2.15
range in projected radius	0:91 - 15:43	0:91 - 15:43	1:00 - 11:90

Table 3. Basic properties of the globular cluster sample

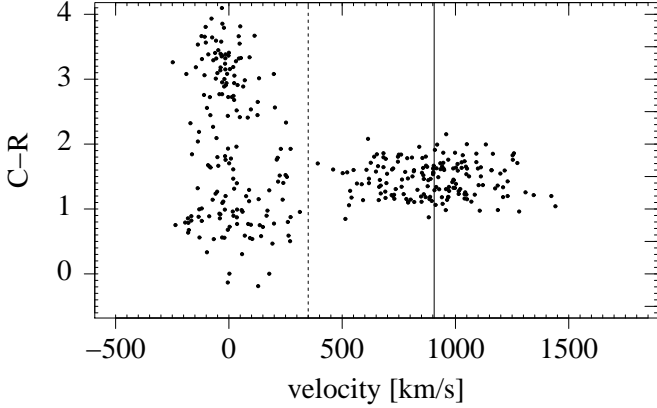


Fig. 4. Color vs. radial velocity. All objects with heliocentric velocities higher than 350 km s^{-1} (dotted line) are regarded as globular clusters. The objects with velocities falling below this limit are foreground stars. The solid line marks the systemic velocity of NGC 4636.

globular clusters. The color magnitude diagram (CMD) for the GCs is shown in Fig. 6. Although the selection of GC candidates was obviously biased towards bright clusters, no clusters brighter than $R = 19$ were found. A few clusters are fainter than $R = 22$, but their velocities have large errors (cf. Fig. 3) and should be considered with caution. Figure 7 shows the histogram of the apparent R-magnitudes for the globular clusters. It illustrates that our spectroscopic study only probes the very bright part of the GCLF, well above the turn-over magnitude at 23.33 (Dirsch et al. 2005). Furthermore, it shows that there is no significant difference between the distributions of blue and red clusters. The magnitude range of the GCs is $19.11 \geq m_R \geq 22.73$ in Kron R. When converted to absolute magnitudes (using the distance modulus of 30.83, Tonry et al. 2001), the globular clusters in our sample span the range $-11.6 \leq M_R \leq -8.1$ in R and $-11.25 \leq M_V \leq -7.6$ in V (for $V - R = 0.47$, Dirsch et al. 2005). Assuming a typical mass-to-light ratio of $M/L_V = 2$, one finds that the masses of the brightest clusters are of the order $7 - 8 \times 10^6 M_\odot$. For comparison: the absolute visual magnitude of ω Centauri (NGC 5139), is $M_V = -10.29$ (Harris 1996) and its mass is about $5 \times 10^6 M_\odot$.

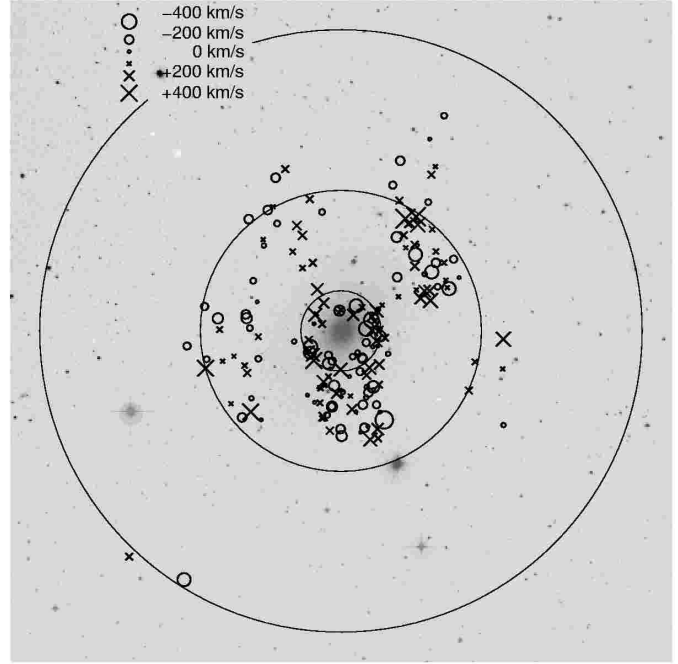


Fig. 5. Spatial distribution of the globular clusters overlaid on a $33' \times 33'$ DSS-image centered on NGC 4636. North is to the top, East to the left. GCs with velocities larger than the systemic velocity of NGC 4636 are marked by crosses. Circles denote GCs with negative relative velocities. The concentric circles have radii of 2, 7, and 15 arcminutes)

5.3. Spatial Distribution

As can be seen in Fig. 5, our target clusters are not uniformly distributed with respect to the center of NGC 4636. At the time of the mask preparation - before the photometric data set was fully analyzed - the projected globular cluster number density was overestimated. Some fields were placed at larger projected distances (see Fig. 1) - at the expense of a more uniform azimuthal coverage. Yet in total, only 15 of the 174 GCs in our sample are found at projected radii larger than $7'.5$. Thus, any measurement of the line-of-sight velocity dispersion beyond this radius is clearly doubtful. Note that the radius at which the power-law index of the projected globular cluster density drops (cf. section 1.2) lies in the range $7'$ to $9'$.

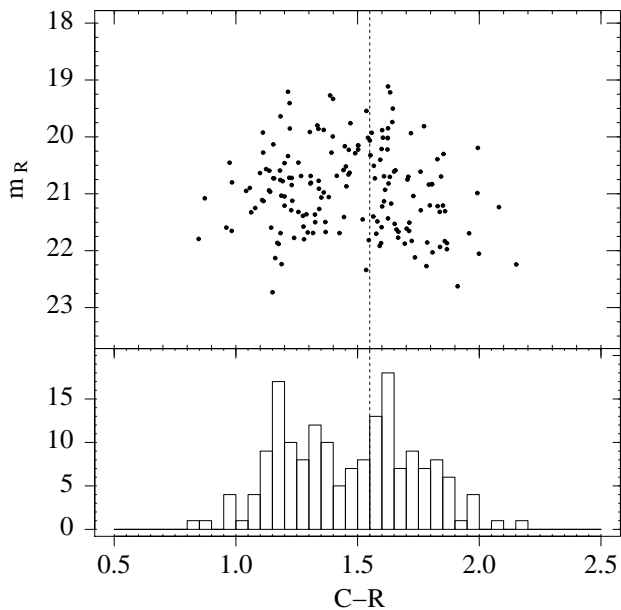


Fig. 6. Top: Color magnitude diagram for the globular clusters. Plotted are C-R vs. R. **Bottom:** Color distribution for the GCs (bin width = 0.05 mag). In both panels, the dotted line at $C - R = 1.55$ indicates the color dividing blue from red clusters (Dirsch et al. 2005).

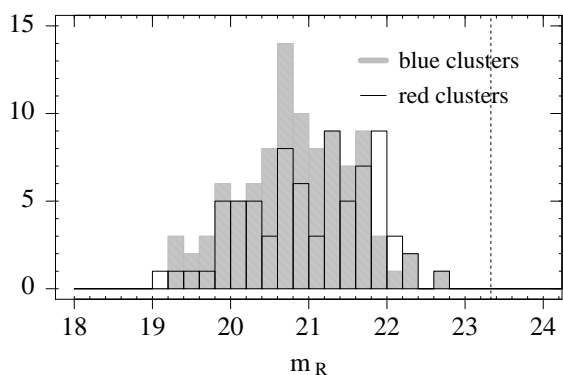


Fig. 7. Globular cluster luminosity distribution (bin width = 0.2 mag). The dotted line at 23.33 indicates the turn-over magnitude of the GCS. Histograms for blue (solid grey) and red clusters.

5.4. Velocity Distributions

In the left panel of Fig. 8 the velocities are plotted against the R magnitudes. As expected, they are found to be concentrated towards the systemic velocity. The brightest clusters however, tend to avoid the systemic velocity. A larger sample is needed to confirm whether this effect is real or due to low-number statistics. The right panel of Fig. 8 shows the velocities plotted against the C-R colors of the clusters. Again, no clear trend is visible, although one notes that the five clusters with the highest velocities are blue. The top right panel of Fig. 9 plots all GC radial velocities versus the projected radii in arcminutes. This figure once more shows how few velocities were obtained for large radii. The more important observation, however, is

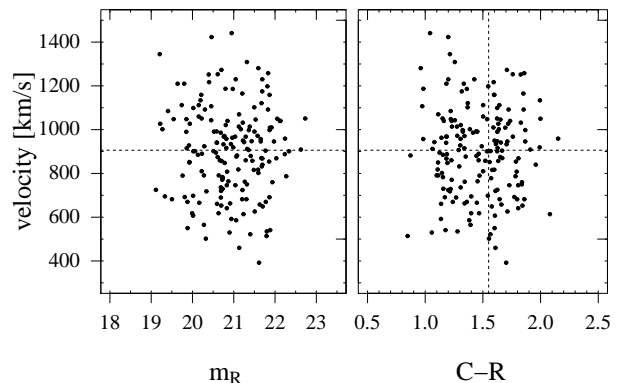


Fig. 8. Left: Radial velocity as a function of apparent R-magnitude. **Right:** Radial velocity of the GCs plotted vs. the C-R-color.

that the scatter of the velocities about the systemic velocity is rather small at a radial distance of about $2' - 4'$. As will be shown later (see section 7), this translates directly into a decrease of the projected velocity dispersion in this radial interval. On the other hand, only relatively few GCs fall into this radial range. The middle and lower right panels of Fig. 9 show the same diagram for blue and red clusters, respectively. In the radial range around $2' - 4'$, the scatter about the systemic velocity is larger for the blue than for the red clusters, hence the radial behavior of the velocity dispersions for the subsamples will turn out to be rather different (see section 7).

6. Rotation

Due to the inhomogeneous azimuthal coverage of our sample it is obvious that statements concerning rotation have to be considered with caution. The diagnostic diagram which we have to analyze is a plot of radial velocities vs. the position angle. Côté et al. (2001) give a useful discussion of the relation between the intrinsic and projected rotational velocity field of a spherical system and we do not repeat that here. If the intrinsic rotation velocity field is stratified on spheres, and the galaxy is not seen pole on, we measure radial velocities that depend sinusoidally on the azimuth angle. Therefore, we fit the following relation :

$$v_r(\Theta) = v_{sys} + A \sin(\Theta - \Theta_0), \quad (1)$$

where v_r is the measured radial velocity at the azimuth angle Θ , v_{sys} is the systemic velocity, and A the rotation amplitude. Figure 10 shows the radial velocities of three samples versus the azimuth angle which goes from North past East. The uppermost panel is the full sample, then follow the blue and the red clusters. A very marginal rotation signal is present in the full sample with the parameters $A = 28 \pm 18 \text{ km s}^{-1}$ and $\Theta_0 = 63 \pm 43$. The blue sample does not show a significant signal ($A = 11 \pm 27 \text{ km s}^{-1}$), while the red sample shows significant rotation, which leaves its imprint on the whole sample. The signal and its significance depends on the color dividing blue and red clusters. The strongest signal is found for clusters redder than $C - R = 1.6$. In this case, we find for the entire red

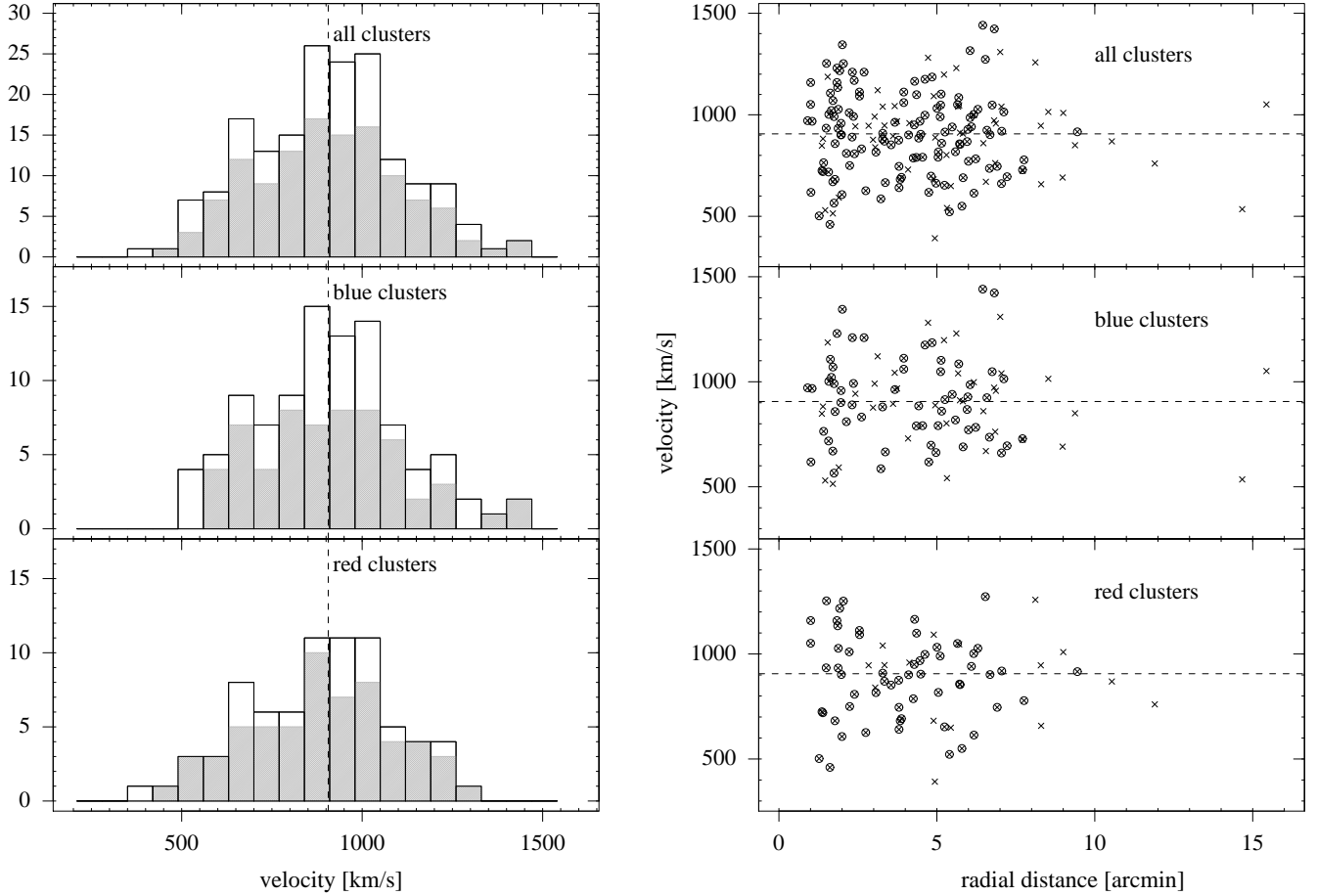


Fig. 9. The left panels show the histograms of the GC velocities for the entire, the blue and the red subsample, respectively. In each panel, the grey histogram shows the distribution of the corresponding error-selected ($\Delta v < 35 \text{ km s}^{-1}$) sample. The dashed line indicates the systemic velocity of NGC 4636, and the bin width is 70 km s^{-1} . The right panels show the radial velocities versus projected galactocentric distance for all, the blue and the red clusters. The crosses in circles denote data points with $\Delta v < 35 \text{ km s}^{-1}$, i.e. they form the error selected samples. Plain crosses denote data points with larger velocity uncertainties. Again, the dashed line marks the systemic velocity of NGC 4636.

sample, $A = -87 \pm 18 \text{ km s}^{-1}$ and $\Theta_0 = 60 \pm 22$, which means a rotation around the minor axis with the southeastern region approaching. Both the amplitude and the position angle remain within the uncertainty limits for subsamples selected in radial bins. Selecting red clusters with projected distances below 5 arcmin, yields $A = -105 \pm 36 \text{ km s}^{-1}$ and $\Theta_0 = 72 \pm 24$. Radii less than 4 arcmin give $A = -114 \pm 44 \text{ km s}^{-1}$ and $\Theta_0 = 72 \pm 25$. However, a confirmation of the rotation of the red clusters is desirable given the relatively low number statistics and the inhomogeneity regarding radius and position angle. Attempts to interpret the rotation, for example, as a dynamical sign for a merger event signs seem therefore premature. In any case, it may be that rotation influences the velocity dispersion of the red clusters, making their use as dynamical tracers more complicated.

7. Velocity Dispersion

The top left panel of Fig. 9 shows the velocity distribution of the entire velocity sample. The bin size was chosen to be 70 km s^{-1} , which is larger than the mean uncertainty. The mean

velocity of $906 \pm 16 \text{ km s}^{-1}$ is in excellent agreement with the systemic velocity of NGC 4636 we determined from the galaxy spectra (cf. section 4.1). The shape of the distribution appears Gaussian (the Anderson–Darling test for normality yields a p -value of 0.81 (Stephens 1974)). This is what one would expect for a kinematical sample that is close to isotropic and in dynamical equilibrium (see e.g. Binney & Tremaine 1987). The most important observable which we want to extract from our data is the projected velocity dispersion and its dependence with radius. Throughout this analysis, it is assumed that our velocity measurements are drawn from one normal distribution. To calculate the velocity dispersions presented in the following section, we employed the maximum-likelihood dispersion estimator presented by Pryor & Meylan (1993). We fixed the systemic velocity of NGC 4636 to $v_{\text{sys}} = 906 \text{ km s}^{-1}$. Then, the velocity dispersion σ is calculated (by iteration) according to:

$$\sum \frac{(v_i - v_{\text{sys}})^2}{(\sigma^2 + \delta_i^2)^2} = \sum \frac{1}{\sigma^2 + \delta_i^2}, \quad (2)$$

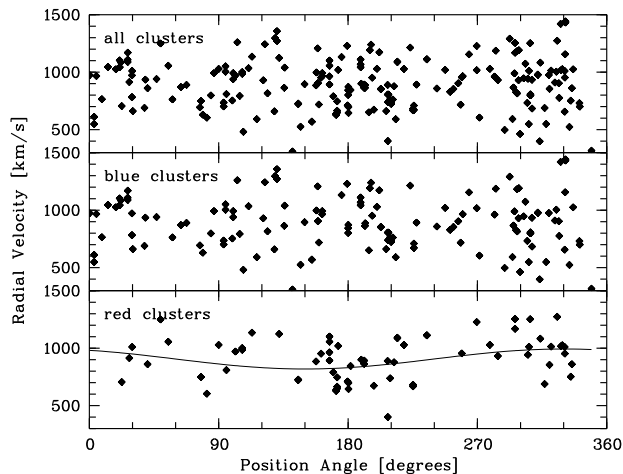


Fig. 10. This plot shows radial velocity vs. the position angle (North past East). The upper panel plots the entire sample, the middle panel the blue clusters and the lower panel the red clusters. A marginal rotational signal is detected in the entire sample, which is due to the stronger signal of the red clusters, which seem to rotate around the minor axis with an amplitude of about 90 km s^{-1} . The blue clusters do not rotate.

where the sum is taken over all velocities and the δ_i are the uncertainties of the individual velocity measurements. The uncertainty of the resulting velocity dispersion is computed according to the expression given by Pryor & Meylan. Calculating the dispersion for all clusters yields: $\sigma_{\text{all}} = 203 \pm 11 \text{ km s}^{-1}$. The velocity dispersions for the blue and red cluster population are $\sigma_{\text{blue}} = 202 \pm 15 \text{ km s}^{-1}$ and $\sigma_{\text{red}} = 199 \pm 17 \text{ km s}^{-1}$, respectively, i.e. they are equal within the uncertainties. In order to study the radial dependence of the velocity dispersion, we chose to divide our samples radial bins of $1'.5$ width. The results are listed in Table 4 and plotted in Fig. 11.

7.1. All Clusters

The upper left panel of Fig. 11 shows the radial dependence of the velocity dispersion for all 170 GCs within $R \leq 9'.0$. For comparison, the line-of-sight velocity dispersion measurements of the central region from Bender et al. (1994) are shown as diamonds. These authors used a long-slit spectrum (with the slit positioned along the major axis) to derive a central velocity dispersion of $\sigma_c = 200 \pm 10 \text{ km s}^{-1}$ and for the average velocity dispersion measured along the major axis ($R < 32''$), they found $\sigma_{\text{maj}} = 200 \pm 30 \text{ km s}^{-1}$. Within the uncertainties, our data points agree with the Bender et al. measurements. Albeit consistent with a constant velocity dispersion of about 200 km s^{-1} , this plot suggests a decrease of $\sigma(R)$ by about 50 km s^{-1} (from ~ 220 to $\sim 170 \text{ km s}^{-1}$) in the radial distance range of roughly $2' - 4'$. To check whether this behavior is merely an artifact produced by velocity measurements with large uncertainties, we next consider an error selected sample ($\Delta v < 35 \text{ km s}^{-1}$) (cf. Fig. 9, lower panel, to see which data points are omitted). The plot for this smaller (120 GC velocities) sample is shown in the upper right panel of Fig. 11. Apparently, the decline is not due to large individual uncertainties. As will be shown next,

R (arcmin)	σ (all) (km s^{-1})	σ (blue) (km s^{-1})	σ (red) (km s^{-1})
no error selection			
1.7	228 ± 23	218 ± 30	241 ± 39
3.2	157 ± 22	160 ± 33	155 ± 32
4.7	204 ± 24	205 ± 33	207 ± 37
6.2	206 ± 25	196 ± 30	190 ± 39
6.2	(169 ± 21)	(126 ± 21)	
7.7	207 ± 43	220 ± 63	196 ± 65
9.2	105 ± 41		
error-selected samples ($\Delta v < 35 \text{ km s}^{-1}$)			
1.7	221 ± 25	198 ± 32	241 ± 38
3.2	185 ± 37	207 ± 64	172 ± 46
4.7	175 ± 24	181 ± 34	168 ± 33
6.2	226 ± 34	227 ± 46	194 ± 42
6.2	(178 ± 27)	(121 ± 27)	
7.7	162 ± 260		
9.2	105 ± 41		

Table 4. Projected velocity dispersion as function of projected galactocentric radius. The upper section shows the values for all, the blue and the red clusters. The dispersions for the corresponding error-selected samples are listed in the lower section. The data are shown in Fig. 11. The values in brackets are those obtained when omitting the two (blue) GCs with velocities above 1400 km s^{-1} .

this pattern is the result of the different behavior of the blue and red subpopulations.

7.2. Blue and Red Clusters

The middle and lower panels of Fig. 11 show the radial dependence of the velocity dispersion for the blue and the red subpopulations, respectively. The values derived for the error selected ($\Delta v < 35 \text{ km s}^{-1}$) samples which consist of 56 blue and 56 red clusters are shown in the right panels. While the blue clusters show a constant velocity dispersion of about 200 km s^{-1} , the velocity dispersion of the red clusters drops from a value of $\sim 240 \text{ km s}^{-1}$ to $\sim 170 \text{ km s}^{-1}$ at a radius of about $2' - 3'$. From this radius on, out to at least $5'.5$, the velocity dispersion apparently remains at the constant, low value. Considering these results for blue and red clusters, one can attribute the drop seen for the whole error selected sample to the red clusters. However, the number of red clusters is rather high in the innermost radial bins, giving the large dispersion at small radii a high degree of confidence. On the other hand, the lower velocity dispersion at larger distances may be uncertain for the individual bins, but that the overall velocity dispersion is lower than for the innermost bin can be stated with high confidence as well. This is a new feature which has not been seen before in any of the few kinematic GC samples of other galaxies. We offer a simple explanation in the context of the spherical Jeans equation in the next section.

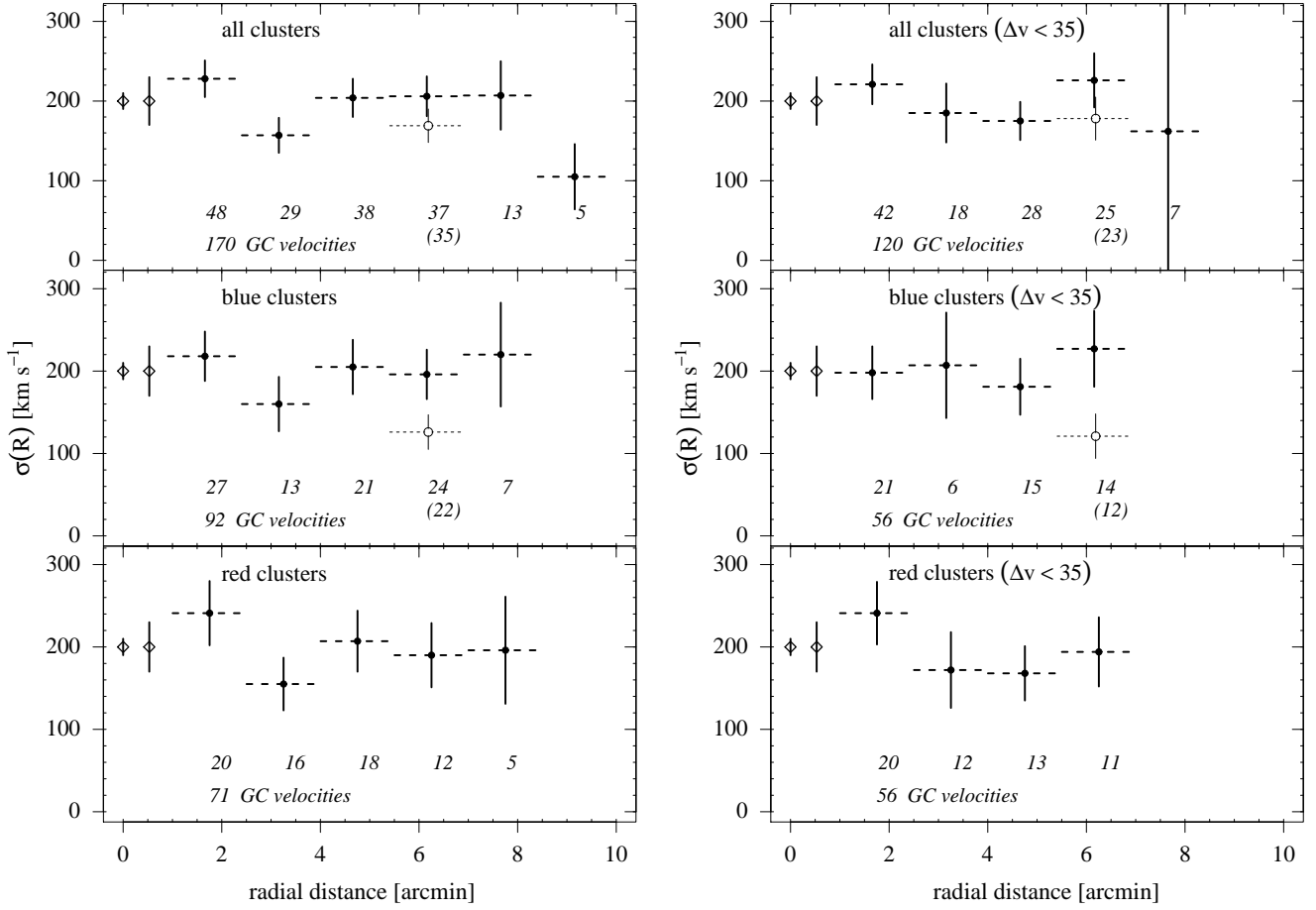


Fig. 11. The left panels show the velocity dispersion versus projected galactocentric radius for the whole, the blue and the red cluster sample, respectively. The right panels show the same for the corresponding error-selected $\Delta v < 35 \text{ km s}^{-1}$ samples. The velocity dispersions were calculated for radial bins of $1'.5$ width, and the number of velocities used for the measurement is shown below each data point. The values plotted here are listed in Table 4. In all panels, the diamonds indicate the dispersion measurements from Bender et al. 1994. The open circles show the dispersion values at $6'$ that are obtained when omitting the two (blue) GCs with velocities above 1400 km s^{-1} .

8. The Mass Profile

The line-of-sight velocity dispersion $\sigma_{los}(R)$ of the globular cluster system and its radial dependence is used to estimate the mass profile of NGC 4636. Given that the number of spectroscopically observed GCs is still far too low for an axisymmetric treatment, we will assume spherical symmetry. This is justified since the deviation from sphericity is modest in the inner parts of the galaxy (Dirsch et al. 2005) where most of our clusters are found. A further argument is the high M/L_B found by Kronawitter et al. (2000) (see 8.3) Given that a flattening in the line of sight leads to an underestimation of M/L (Magorrian & Ballantynes 2001), it is hard to imagine that such a high value is still underestimated.

8.1. The Mass Profile from the Jeans Equation

The collisionless Boltzmann equation is used to derive the spherical, non-rotating Jeans equation (see Binney & Tremaine 1987 for a full treatment).

$$\frac{d(\ell(r)\sigma_r(r))}{dr} + 2\frac{\beta(r)}{r}\ell(r)\sigma_r(r) = -\ell(r)\frac{G \cdot M(r)}{r^2} \quad (3)$$

$$\text{with } \beta \equiv 1 - \frac{\sigma_\theta^2}{\sigma_r^2}.$$

Here, r is the radial distance from the center and ℓ is the spatial (i.e. three-dimensional) density of the GCs; σ_r and σ_θ are the radial and azimuthal velocity dispersions, respectively. β is the anisotropy parameter, and G is the constant of gravitation. To derive the enclosed mass $M(r)$, one needs to know β . In other words: the potential and the anisotropy are degenerate in the spherical approximation. Information about the anisotropy must be inferred from higher moments of the velocity distribution, for which one needs much larger samples than ours. Merritt & Tremblay (1993) used M 87 as an example and esti-

mated that several hundred, perhaps thousand velocities would be required to detect a velocity anisotropy.

8.2. The Jeans–Analysis: Principle

For our analysis we use the expressions given by e.g. Mamon & Łokas (2005) (see also van der Marel (1994)). Given a mass distribution $M(r)$, a three–dimensional mass or number density of a tracer population $\ell(r)$, and a *constant* anisotropy parameter β , the solution to the Jeans equation (Eq. 3) reads:

$$\ell(r) \sigma_r^2(r) = G \int_r^\infty \ell(s) M(s) \frac{1}{s^2} \left(\frac{s}{r}\right)^{2\beta} ds \quad (4)$$

This expression is then projected using the following integral:

$$\sigma_{\text{los}}^2 = \frac{2}{I(R)} \left[\int_R^\infty \frac{\ell \sigma_r^2 r dr}{\sqrt{r^2 - R^2}} - R^2 \int_R^\infty \frac{\beta \ell \sigma_r^2 dr}{r \sqrt{r^2 - R^2}} \right] \quad (5)$$

where $I(R)$ is the projected number density of the tracer population.

8.3. Luminous Matter

To assess the mass distribution of the luminous (stellar) component, we proceed as follows: The photometric study by Dirsch et al. (2005) provides a surface brightness profile in Kron-Cousins R. It reads:

$$\mu(R) = -2.5 \log \left(a_1 \left(1 + \frac{R}{R_1} \right)^{-\alpha_1} + a_2 \left(1 + \frac{R}{R_2} \right)^{-\alpha_2} \right), \quad (6)$$

with $a_1 = 3.3 \times 10^{-7}$, $R_1 = 0.11'$, $\alpha_1 = 2.2$, $a_2 = 5.5 \times 10^{-9}$, $R_2 = 8.5'$, and $\alpha_2 = 7.5$. To obtain the luminosity density [L_\odot/pc^3], the intensity profile $I(R) = 10^{-0.4\mu(R)}$ has to be deprojected. This was done using the Abel deprojection integral (Eq. 7). For the cutoff–radius r_t , we chose a value of $2000''$, roughly twice the distance of the last photometric datapoint.

$$\varepsilon(r) = -\frac{1}{\pi} \left[\int_r^{r_t} \frac{dI(R)}{dR} \frac{dR}{\sqrt{R^2 - r^2}} - \frac{I(r_t)}{\sqrt{r_t^2 - r^2}} \right] \quad (7)$$

Further assumptions are spherical symmetry, and a distance of 15 Mpc. Moreover, we have to take into account that we use an R-surface brightness profile: in order to translate it into solar luminosities, we need the absolute magnitude of the Sun in this filter. We use a value of $V - R = 0.370$ (Bessell et al. 1998) for the Sun, i.e. $M_{R,\odot} = 4.46$. The deprojected luminosity density was then (numerically) integrated to yield a cumulative luminosity (in units of L_\odot). The latter was fit by a sixth–order polynomial $\sum m_i \cdot R^i$ (R in parsec) with the coefficients: $m_0 = 6.38 \times 10^8$, $m_1 = 3.22 \times 10^6$, $m_2 = -70.0$, $m_3 = 5.62 \times 10^{-4}$, $m_4 = 3.54 \times 10^{-9}$, $m_5 = -8.92 \times 10^{-14}$ and $m_6 = 4.22 \times 10^{-19}$. The polynomial is a good representation in the range $2 < R < 70$ kpc.

To convert the cumulative luminosity into a mass profile, the stellar mass-to-light ratio is required, i.e. M/L_R . Kronawitter et al. (2000) quote a value of $M/L_B = 9$ for a distance of 20.5 Mpc. Because M/L is inversely proportional to the distance, one has to apply a factor of 1.36 to get $M/L_B = 12.2$ at a

distance of 15 Mpc. This value is suspiciously high. Although it formally fits old, metal-rich populations with steep mass functions, Bell et al. (2003) quote $M/L_B = 10$ as an upper limit found for their large 2MASS-sample. According to their relation of (B-R) versus M/L_B , NGC 4636 would have an M/L_B of approximately 6. Further uncertainties are the distance (Dirsch et al. 2005) and the tangential anisotropy (Kronawitter et al. 2000) of NGC 4636. Obviously, there is some freedom in adopting the mass-to-light-ratio of the stellar population. First we assume $M/L_B = 12.2$, according to Kronawitter et al., but we shall also consider other values. In order to transform this mass-to-light ratio into an M/L_R value, one has to apply the factor of $10^{-0.4((B-R)_{4636} - (B-R)_\odot)}$. With $(B - R)_{4636} = 1.6$ and $(B - R)_\odot = 0.97$, a factor of 0.56 results, hence $M/L_R = 6.8$. Further, we make the assumption that M/L_R of the stellar light is constant for the entire galaxy. This is justified since the color gradient of NGC 4636 is relatively shallow ($\Delta(C - T) \simeq -0.1$ in the range $0.5 - 4'$), and the stellar populations seem to be well mixed (Dirsch et al. 2005).

For our modeling (cf. Sect. 8.6), we assume that the stellar mass is contained within 70 kpc, yielding $M_{\text{stars}} = 4.2 \times 10^{11}$ and $2.6 \times 10^{11} M_\odot$ for $M/L_R = 6.8$ and 4.3, respectively. The lower value shall illustrate the dependence on M/L . We adopt $M/L_V = 5.5$ from Loewenstein & Mushotzky (2003) which results in $M/L_R = 4.3$.

8.4. Blue GCs as Tracer Population

Since the projected number density $N(R)$ of the blue globular clusters follows a double power–law, the de–projection is somewhat tricky. We proceeded as follows: following Zhao (1997) we adopt a double power–law as

$$N(R) = n_0 \left(\frac{R}{B} \right)^{-\gamma_1} \left[1 + \left(\frac{R}{B} \right)^{1/\alpha_1} \right]^{-(\beta_1 - \gamma_1)\alpha_1}. \quad (8)$$

Capitals mean values in projection. $\gamma_1, \beta_1, \alpha_1$ are the slope of the inner power–law, the slope of the outer power–law, and the width of the transition region, respectively. B is a scale radius. This function was fitted to the number–counts, resulting in $n_0 = 8.02 \text{ GCs} \times \text{arcmin}^{-2}$, $B = 8.86'$, $\gamma_1 = 0.33$, $\beta_1 = 7.19$, $\alpha_1 = 0.54$.

This function was then deprojected using Eq. 7 and in turn fitted with the same function, resulting in $n_0 = 0.38 \text{ GCs} \times \text{arcmin}^{-3}$, $b = 8.86'$, $\gamma_1 = 1.0$, $\beta_1 = 7.71$, $\alpha_1 = 0.4$.

As a check, this 3D-profile was re–projected, using the Abel projection operator

$$I(R) = 2 \int_R^{r_t} \frac{\varepsilon(r) r dr}{\sqrt{r^2 - R^2}} \quad (9)$$

and found to be in good agreement with our 2D data (see Fig. 12).

For simplicity, the anisotropy parameter β is assumed to be constant with radius. With our limited sample we cannot put any constraints on possible radial variations of β .

As a tracer population we choose the error-selected blue clusters. The red clusters show a more complex behavior. They seem to rotate, their projected number density is best described

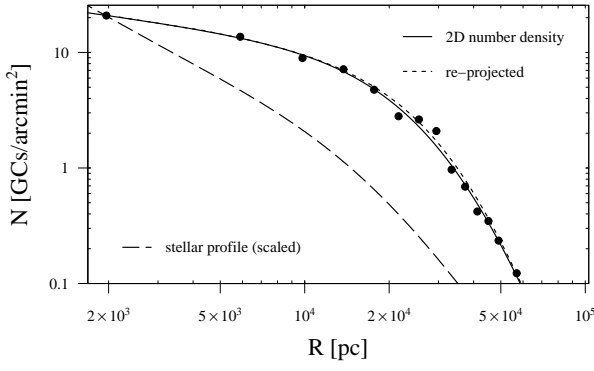


Fig. 12. Projected radial number density of blue GCs. The data points are from Dirsch et al. (2005), the solid line is the a double power-law (cf. Eq. 8) fit to the data and the dashed line is the re-projected 3D number-density. It deviates only marginally from the 2D-fit. For comparison we also show the projected light profile according to Dirsch et al. (2005).

by three power-laws, and the projected velocity dispersion also shows more complex features. Therefore, we postpone any inclusion of the red clusters in the dynamical analysis until more data becomes available.

But also the blue clusters pose problems. As can be seen in Fig. 11 and Fig. 9, the velocity dispersion value of the outermost bin is strongly affected by two outliers. Including those objects one obtains $227 \pm 46 \text{ km s}^{-1}$ instead of $121 \pm 27 \text{ km s}^{-1}$. The high value would mean an almost constant dispersion out to 7 arcmin. As seen later on this would be inconsistent with a sharp drop of the cluster system at this radius. This unsatisfactory situation can as well only be remedied with future data. For now, we calculate our models for both values. This argument cannot be transferred easily to the red clusters. If they rotate, a constant velocity dispersion is plausible since we average azimuthally.

8.5. Dark matter

For the dark component we adopt a density profile of the form:

$$\rho_{\text{dark}} = \rho_{\text{dark},0} \left(\frac{r}{r_{\text{dark}}} \right)^{-1} \left(1 + \frac{r}{r_{\text{dark}}} \right)^{-2}. \quad (10)$$

i.e. an NFW profile (Navarro et al. 1997, Bullock et al. 2001). For this density profile, the cumulative mass $M(r)$ reads

$$M_{\text{dark}} = 4\pi \cdot \rho_{\text{dark},0} \cdot r_{\text{dark}}^3 \cdot \left(\log \left(1 + \frac{r}{r_{\text{dark}}} \right) - \frac{\frac{r}{r_{\text{dark}}}}{1 + \frac{r}{r_{\text{dark}}}} \right). \quad (11)$$

The task is now to find values for the characteristic density $\rho_{\text{dark},0}$ and the characteristic radius r_{dark} resulting in a dark component which, when added to the luminous matter can reproduce the observed projected velocity dispersion in the radial range of the globular clusters.

8.6. Results

Having chosen a value for the stellar M/L and β , we calculate according to Eq. 4 the product of radial velocity dispersion

squared and the 3-dimensional number density. This we project according to Eq. 5. For each pair of M/L and β , we vary the dark matter parameters ($r_{\text{dark}}, \rho_{\text{dark},0}$), until the projected model dispersion shows minimal residuals with regard to the observed dispersion. For simplicity, the four data points were given equal weights and the residuals were calculated using

$$\text{r.m.s} = \sqrt{\frac{\sum (\sigma_{\text{model}} - \sigma_{\text{los}})^2}{n}}. \quad (12)$$

We defined a set of radii ($r_{\text{dark}} \in \{5, 10, 40, 80, 120, 240\}$ kpc) for which we then adjusted the density. Table 5 lists the model parameters together with derived quantities such as the virial mass and radius, the M/L_R-values, and the dark matter fractions within 30 kpc and 7.5 kpc (the effective radius). We determined the virial radius according to the Bullock et al. definition (i.e. at R_{vir} , the mean density of the halo is 337 times the mean mass density of the universe, $\rho_0 \cdot \Omega_m$). Note that the virial quantities were calculated for the dark component alone, with the aim of comparing their properties to those of simulated N-body halos (cf. Sect. 9.1). Thus, having omitted the stellar component, the virial masses are lower limits.

Our models are displayed in Figs. 13 and 14, which show our analysis for the two different stellar M/L_R-values of 6.8 and 4.3, respectively. Table 5 lists the halo parameters. The left and right panels refer to the difference in the last data bin as seen in the topmost panels which show the comparison between our models and the data. The observed velocity dispersion together with their statistical uncertainties are indicated. We emphasize the importance of the uncertain outermost bin which is clearly dominated by systematics as mentioned above. The various anisotropic models are distinguished by different line styles which can be identified in the second panel which shows the associated dark matter circular velocities. The degeneracy of potential and anisotropy is nicely visible. Only the models without dark matter, which are shown separately in Fig. 15 seem to be excluded.

The third panels show the total circular velocities, i.e. the sum of dark and luminous matter. The stellar component is indicated with a dotted line. The circular velocity values derived by Kronawitter et al. are shown as circles. Since our stellar mass-to-light ratio of 6.8 was adopted from the Kronawitter et al. analysis, it is not surprising that they do not fit well in the case of M/L=4.3.

The bottom panels show the radial dependence of the corresponding M/L_R-values (cf. Table 5 for a listing of mass-to-light ratios at $R = 30$ and 7.5 kpc).

Of course, since the stellar M/L-value enters as a free parameter, the dark matter fraction would rise with declining M/L. However, M/L_R = 4.3 is already low for an old, metal-rich stellar population. Further constraints on the M/L ratio have to come from a more precise analysis of the dynamics of the stellar body.

In all four model families, the $\beta = 1$ (i.e. totally radial) models perform worst. Besides being a poor fit to the data, these models require very massive ($M_{\text{vir}} > 10^{13} M_{\odot}$) and extended dark matter halos.

The observed GC velocity dispersion (calculated omitting the two extreme velocities) as shown in the left panels of

Table 5. Parameters of the dark matter halos. The first columns labels the models. The mass-to-light ratio M/L_R and the dark matter fraction are calculated for two radii (7.5 kpc $\approx R_{\text{eff}}$ and 30 kpc is the radius within which the GCs used in the analysis are found). From the NFW parameters of our model halos, we calculate the virial radius, mass and the concentration parameter ($c_{\text{vir}} = R_{\text{vir}}/r_{\text{dark}}$) using the definitions of Bullock et al. (2001). Then we give the total mass within 30 kpc, mass-to-light ratios (R-band) and the dark matter fraction within 30 kpc and 7.5 kpc (effective radius). Note that the virial quantities were calculated for the dark halos without adding the stellar component. Thus, the virial masses presented below are lower limits.

#	β	r_{dark} [kpc]	$\varrho_{\text{dark},0}$ [$M_{\odot} \text{pc}^{-3}$]	r.m.s [km s^{-1}]	R_{vir} [kpc]	M_{vir} [$10^{12} M_{\odot}$]	c_{vir}	$M_{<30\text{kpc}}$ [$10^{11} M_{\odot}$]	M/L_R ($r = 30 \text{ kpc}$)	$\frac{M_{\text{dark}}}{M_{\text{total}}}$ ($r = 30 \text{ kpc}$)	M/L_R ($r = 7.5 \text{ kpc}$)	$\frac{M_{\text{dark}}}{M_{\text{total}}}$ ($r = 7.5 \text{ kpc}$)
$M/L_R = 6.8, \sigma_{\text{los}}(27 \text{ kpc}) = 121 \text{ km s}^{-1}$ (cf. Fig. 13, left panels)												
1	-2.0	5	0.12	23	207	0.52	41.4	5.5	10.9	0.37	9.6	0.29
2	-0.5	10	0.033	20	255	0.96	25.5	5.5	12.0	0.43	9.4	0.27
3	0	40	0.003	21	395	3.6	9.9	6.6	13.1	0.48	8.4	0.19
4	0.5	120	0.00075	26	655	16.6	5.5	7.2	14.3	0.52	8.2	0.17
5	1.0	240	0.00050	46	1100	77.9	4.57	9.2	18.3	0.63	8.7	0.22
$M/L_R = 4.3, \sigma_{\text{los}}(27 \text{ kpc}) = 121 \text{ km s}^{-1}$ (cf. Fig. 14, left panels)												
6	-2.0	5	0.195	22	248	0.90	49.6	5.5	10.9	0.61	8.9	0.52
7	-0.5	5	0.230	20	264	1.01	52.8	6.1	12.1	0.64	9.7	0.56
8	0	20	0.0135	20	358	2.7	17.9	5.3	10.6	0.59	5.9	0.27
9	0.5	120	0.00100	25	743	24.1	6.2	7.2	14.3	0.70	6.2	0.30
10	1.0	120	0.00145	45	870	39.0	7.3	9.4	18.7	0.77	7.0	0.37
$M/L_R = 6.8, \sigma_{\text{los}}(27 \text{ kpc}) = 227 \text{ km s}^{-1}$ (cf. Fig. 13, right panels)												
11	-2.0	120	0.0012	18	803	30.5	6.7	9.4	18.7	0.64	9.0	0.25
12	-0.5	80	0.0019	25	650	16.0	8.1	9.0	26.7	0.75	10.5	0.35
13	0.0	120	0.0011	32	773	27.2	6.4	9.0	17.7	0.62	8.8	0.23
14	0.5	120	0.0012	47	803	30.5	6.7	9.5	18.7	0.64	9.0	0.25
$M/L_R = 4.3, \sigma_{\text{los}}(27 \text{ kpc}) = 227 \text{ km s}^{-1}$ (cf. Fig. 14, right panels)												
15	-2.0	80	0.0023	16	703	20.4	8.8	9.0	18.0	0.76	7.1	0.39
16	-0.5	120	0.0011	24	774	27.3	6.5	7.7	15.2	0.72	6.3	0.32
17	0.0	120	0.00135	27	845	35.4	7.0	9.0	17.7	0.76	6.8	0.37
18	0.5	120	0.0014	42	858	37.0	7.15	9.2	18.2	0.76	6.9	0.38

Figs. 13 and 14 can be reproduced for a range of anisotropy parameters ($-2 < \beta < 0.5$). The tangential models result in less massive and more concentrated dark halos. The isotropic model has a virial radius of about 360–400 kpc (depending on the stellar M/L value) which is compatible to the extent of the X-ray emission.

Although the virial masses of the dark halos differ by more than one order of magnitude, the total mass within the radial range probed by the GC dynamics changes by only a factor of 1.5.

Hence, we can put constraints on the amount of dark matter in NGC 4636 within 30 kpc ($\approx 4 R_{\text{eff}}$), while the shape of the halo remains largely unknown.

For completeness we also included in our analysis the values of $\sigma_{\text{los}}(R)$ obtained when including extreme velocities of two GCs in the last radial bin. The resulting almost constant line-of-sight velocity dispersion of the GCs as shown in the right panels of Figs. 13 and 14 can only be reproduced with a very extended dark matter component. The best agreement in the sense of lowest residuals is found for the $\beta = -2$ tangential models. The radial $\beta = 0.5$ models provide rather poor fits, and the case of completely radial orbits $\beta = 1$ (not shown) appears even worse.

9. Discussion

9.1. Comparison to Cosmological Simulations

How do our model dark matter halos compare to cosmological N-body simulations? Is such a comparison meaningful? Particularly the less massive halos are expected to have experienced contraction during the galaxy formation process. On the theoretical side, the universality of dark matter halos is still under discussion (see Reed et al. 2004 and references therein) so that a possible disagreement may not provide a solid basis for deeper conclusions. We therefore refrain from lengthy considerations and only point out basic tendencies.

For comparison with simulations we choose the study of Bullock et al. (2001). They analyzed a sample of ~ 5000 simulated halos in the range $10^{11} - 10^{14} M_{\odot}$. They found (like others) that the concentration parameter c_{vir} decreases with growing mass, but the scatter in the halo profiles for a given mass is still quite large. A comparison with Fig. 4 of Bullock et al. shows that for our model family shown in the left column of Fig. 13 (i.e. $M/L_R = 6.8$, omitting the two extreme blue clusters), the $\beta = 0$ halo (model 3) fits best to the simulations. The halos corresponding to the models with tangential bias have higher concentration parameters than halos of the same mass shown by Bullock et al., but may be still consistent. The models with

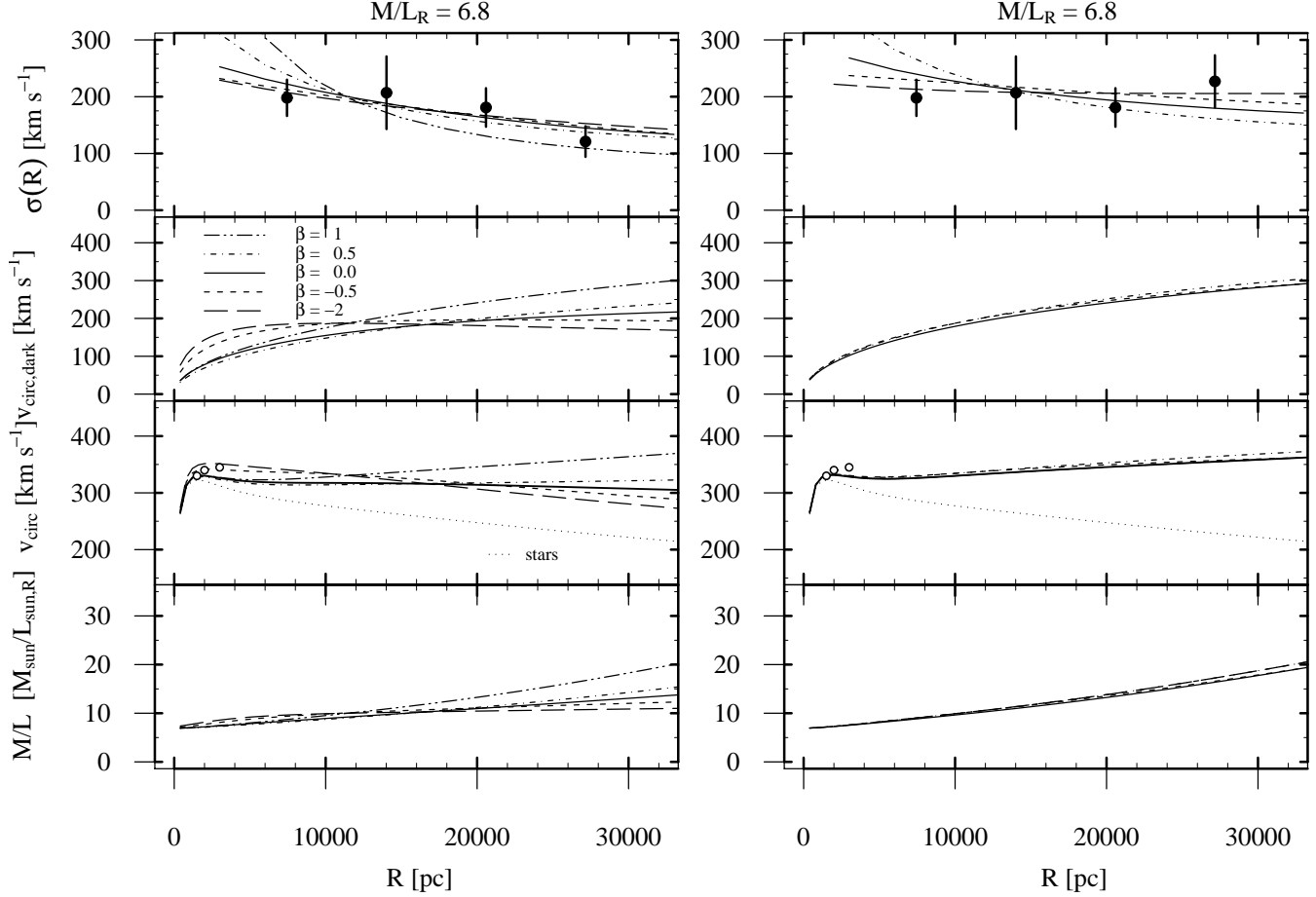


Fig. 13. Mass models for a stellar M/L -ratio of 6.8. The left and right panels are distinguished by the value of the last bin. The topmost panels show the measured velocity dispersions (cf. Fig. 11 and Table 4) together with the modelled line-of-sight velocity dispersions. The second panels show the circular velocity curves of the dark matter components. Below that, the circular velocity curves for the sum of luminous and dark matter are shown. The circular velocity of the stars alone is shown as dotted line. Circles show the values derived by Kronawitter et al. (2000). The mass to light-ratio as a function of radius is shown in the bottom panels. Different line types indicate results for different anisotropy parameters as labeled in the second panel on the left.

radial anisotropies have small concentration parameters, but are as well not excluded. This is true even for the completely radial models (which give the worst fits to the observations). The question therefore is whether, given the large range of permitted halo shapes indicated by the simulations, one can meaningfully compare at all theoretical simulations with observations of our kind, not to mention the complications if dissipative effects of galaxy formation are taken into account. All we can say is that our model halos do not contradict the simulations of Bullock et al.

9.2. Mass Profile and Comparison with X-ray Mass Profiles

NGC 4636 has recently been a target for various X-ray studies (e.g. O’Sullivan et al. 2005, Ohto et al. 2003, Xu et al. 2002, Jones et al. 2002), emphasizing the highly disturbed X-ray pattern. However, mass profiles derived from X-rays are until now published only by Matsushita et al. (1998) and Loewenstein & Mushotzky (2003). Figure 16 shows the various mass profiles.

The two solid lines are our models with the lowest and the highest mass within 30 kpc (models 1 and 14). The dotted line is the model with the highest dark matter content within one effective radius (model 7). The long-dashed line is the mass profile from Loewenstein & Mushotzky (2003). The total mass enclosed within 30 kpc is for the latter profile $1.25 \times 10^{12} M_{\odot}$, distinctly higher than our highest value. Furthermore, the mass profile is steeper than most of our models, rising as $R^{1.2}$. However, a very concentrated dark halo, even surpassing this X-ray profile at small radii, is not excluded. One can speculate that the difference at larger radii might have to do with different hydrodynamical situations at small and large radii.

The dashed-dotted line is the mass profile from Matsushita et al. 1998 (based on ASCA data), read off from their log-log diagram (their Fig. 3, solid line, scaled down to our distance of 15 Mpc) which shows most distinctly the flattening of the mass profile at 10 kpc radius. However, their range of mass profiles consistent with the X-ray analyses is rather large, apparently including the possibility that there is no such flattening. In their work, NGC 4636 is extremely dark matter dominated, the lu-

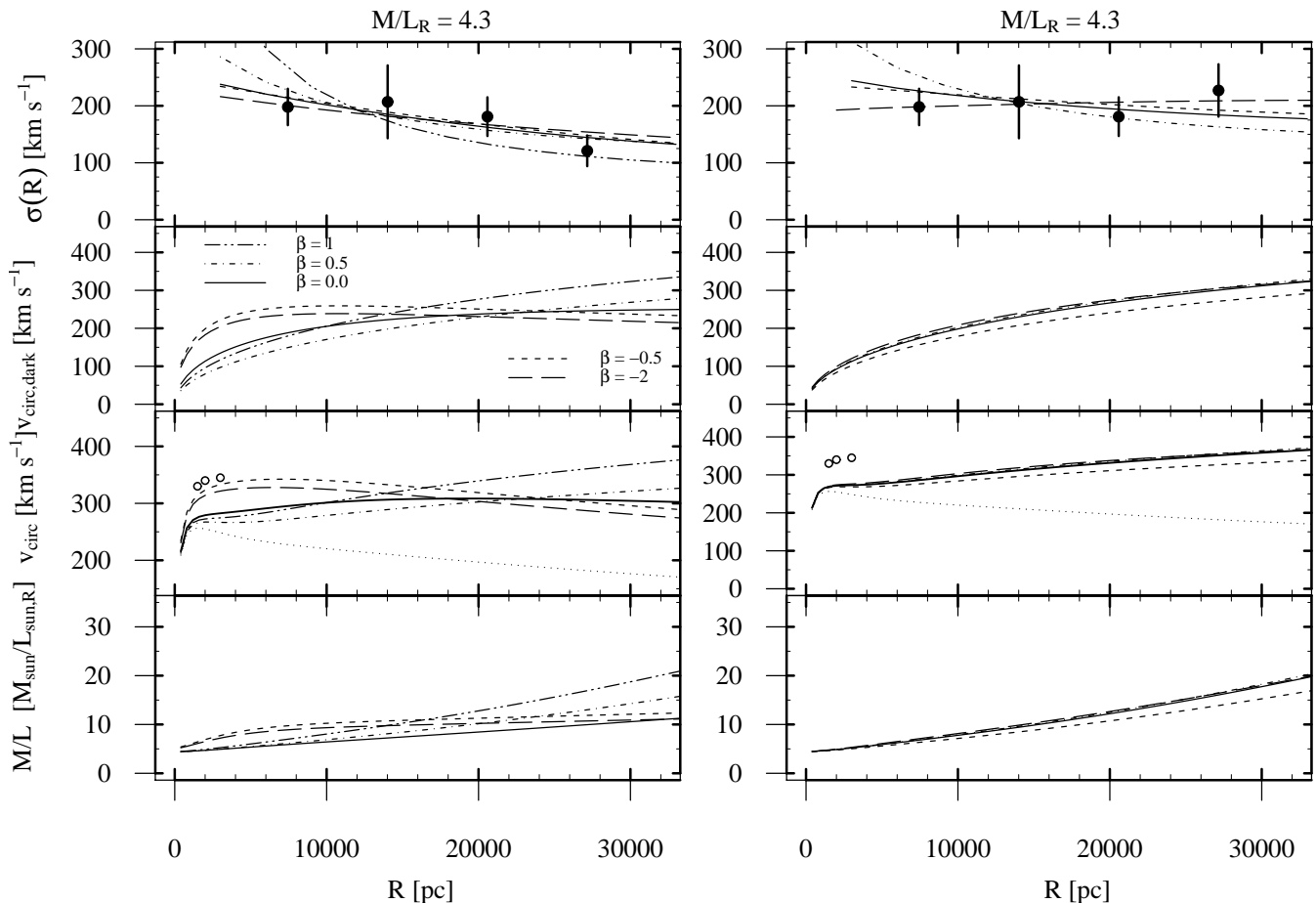


Fig. 14. Same as Fig. 13, but for a lower stellar M/L -ratio of 4.3. See Table 5 for the model parameters.

minous mass falling short by a factor of 2-3 already at small radii. Matsushita et al. quote $M/L = 8$ for the stellar component but give neither the band nor the source of their photometry, so we cannot comment further on that. The agreement with the GC analysis out to 10 kpc is reasonably good. Outside this radius, the discrepancy is caused by the flattening of the profile for which we see no indication. A similar flattening of the mass profile has been observed with ASCA in the cases of NGC 1399 (Ikebe et al. 1996) and in Abell 1795 (Xu et al. 2002). However, it has not been seen in the ROSAT data for NGC 1399 (Jones et al. 1997). Jones et al. (2002) interpret the high X-ray luminosity of NGC 4636 as the transient phenomenon of an enhanced cooling rate. Hence it is possible that the total gravitating mass of this galaxy cannot be accurately determined from the X-ray emission. An interesting point is the large radial extension of the X-ray emission found by ASCA. If the dark matter fraction in NGC 4636 is low then this emission might indicate a dark halo not related to NGC 4636 itself. One could speculate about a dark substructure in the general Virgo potential, formerly hosting a galaxy group which formed NGC 4636 as the result of the merging of several galaxies. The quite abrupt termination of the GC system between $7'$ - $9'$ would speak in favor of this scenario. Stars or GCs, respectively, near their escape energy are expected to show a drop in their radial density profile. If NGC 4636 was embedded in a deep dark matter

potential reaching smoothly out to large radii then one would expect to find GCs at large radii which are still bound to NGC 4636 and accordingly a sharp boundary would not fit into the picture. However, it is interesting to note that the blue clusters apparently do not trace the dark halo, as has been suggested for other galaxies, e.g. NGC 1399 (Forte et al., 2005). Deeper insight could come from a more complete sampling of GCs or Planetary Nebulae at or beyond a radius of $9'$, which will be a difficult observational task.

9.3. Modified Newtonian Dynamics

The CDM paradigm is the most widely accepted view onto structure and galaxy formation. Alternative concepts to explain the kinematics of galaxies without resorting to dark matter are until today minority views. One of these alternative concepts is Modified Newtonian Dynamics (MOND) which one finds to be discussed with increasing intensity. (e.g. Milgrom 1983, Sanders & McGaugh 2002). As a phenomenological recipe, the Newtonian acceleration \mathbf{g}_N has to be replaced by the MOND acceleration in the case of small accelerations \mathbf{g} through the relation

$$\mathbf{g}_N = \mu(g/a_0) \cdot \mathbf{g}, \quad (13)$$

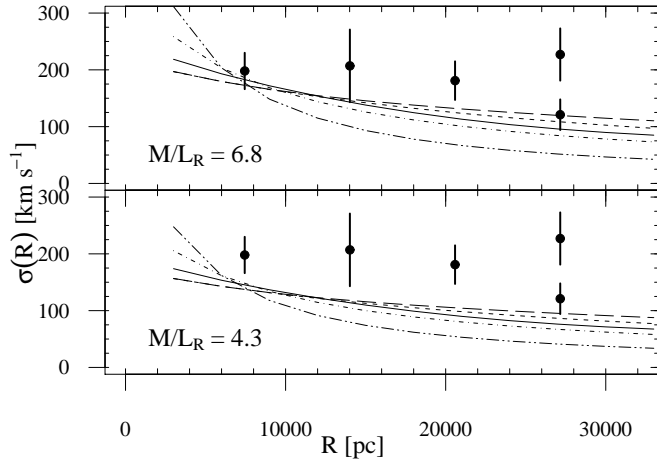


Fig. 15. Projected velocity dispersions for models *without* dark matter. Upper panel: $M/L_R = 6.8$, lower panel: the same for a stellar mass-to-light ratio of $M/L_R = 4.3$. The line styles are the same as in Figs. 13 and 14, i.e. the solid lines correspond to $\beta = 0$, the long and short dashed lines to the tangential models $\beta = -\frac{1}{2}, -2$, respectively. The radial models $\beta = \frac{1}{2}, 1$ are shown as dot-dashed and dot-dot-dashed lines. Only the models with a high stellar mass-to-light ratio in conjunction with tangential anisotropies are marginally consistent with the measured line-of-sight velocity dispersions.

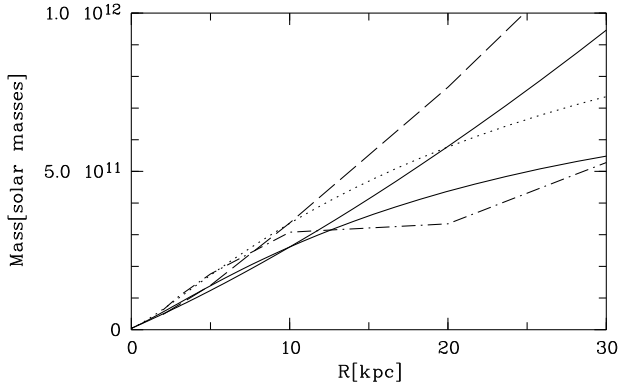


Fig. 16. Various mass profiles. This graph shows various mass profiles of NGC 4636. The solid lines are the models with the lowest and highest mass within 30 kpc, respectively (models 1 and 14). The dotted line is the model with the highest dark matter content within 30 kpc (model 7). The dashed-dotted line approximates one mass profile from Matshushita et al. (1998), showing the flattening at about 10 kpc. The long-dashed line represents the mass profile from Loewenstein & Mushotzky (2003). See text for more details.

with

$$a_0 \approx 1.2 \cdot 10^{-8} \text{ m} \cdot \text{s}^{-2}$$

being a universal constant and $\mu(g/a_0)$ an unspecified function interpolating between the Newtonian and the MOND regime. Bekenstein & Milgrom (1984) presented a Lagrangian formalism of MOND. In case of a spherical mass distribution this formalism reduces to the above simple formula.

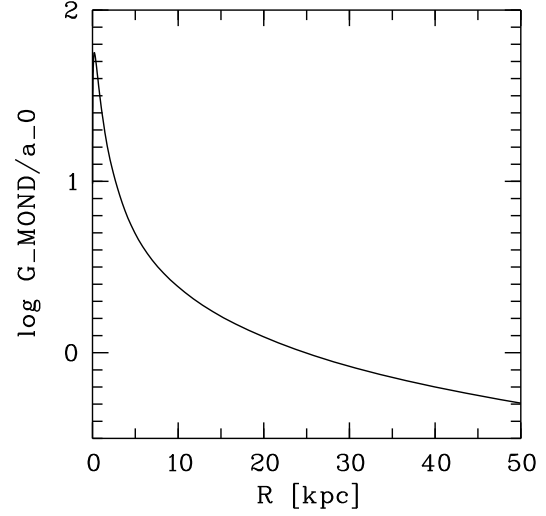


Fig. 17. This graph shows the ratio of the MONDian acceleration to a_0 as a function of galactocentric radius. Equality is reached at about 30 kpc which already is the limit of our investigation. This means that the deep MOND regime cannot be reached by dynamical tracers and that the scheme of interpolating between the MONDian and the Newtonian regime dominates the analysis. A stellar mass-to-light ratio of $M/L_R = 6.8$ was assumed.

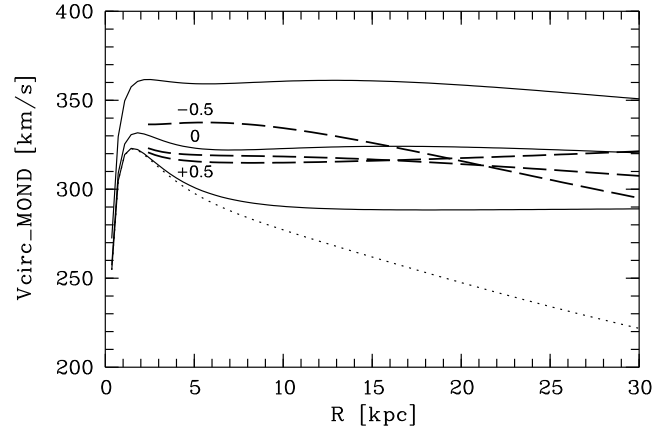


Fig. 18. MOND rotation curves for different interpolation schemes are shown for a stellar M/L_R ratio of 6.8 (solid lines). The upper solid line is derived from Bekenstein's interpolation, the middle one from Famaey & Binney's, and the lower one from the "standard" interpolation (see text for explanation). The dashed lines indicate the derived circular velocities from GCs for the given anisotropy parameters (models 3,4,5). The dotted line is the stellar component alone with an adopted $M/L_R = 6.8$. The Famaey & Binney interpolation apparently works best.

MOND proved to have an impressive predictive power (e.g. Sanders & McGaugh 2002). Many arguments have been raised against MOND, including its apparent arbitrariness, but until now no convincing case has been found which would disprove MOND. Meanwhile, MOND also has a theoretical foundation in the work of Bekenstein (2004). Perhaps the most serious ob-

jection is that MOND does not remove the need for dark matter on cluster scales (Sanders 2003, Pointecouteau & Silk 2005). However, ignoring pro's and contra's for the moment, we want to see MOND's performance in the case of NGC 4636.

MOND works successfully in the cases of spiral galaxies and dwarf galaxies. Giant ellipticals are more difficult test objects due to the fact that MOND effects start to become visible at radii where the low surface brightness is an obstacle for reliable investigations of the galaxy's dynamical behavior. However, Gerhard et al. (2001), in their sample of 21 elliptical galaxies, found the onset of increasing M/L -values at accelerations, which are a factor of 10 higher than in spiral galaxies. This would remove the universal character of a_0 . Milgrom & Sanders (2003) counterargued that there were discrepancies between Gerhard et al.'s analysis and that of Romanowsky et al. (2003), indicating that the last word has not been spoken yet. Therefore, it is interesting to have a look at the MOND rotation curve of NGC 4636, expected from the luminosity density profile and a certain M/L -ratio.

Figure 17 shows the ratio of the MOND acceleration to a_0 in dependence on radial distance (for the "standard" interpolation function mentioned hereafter). An M/L_R -ratio of 6.8 has been adopted. The graph shows that giant elliptical galaxies like NGC 4636 are nowhere in the deep MOND regime. Thus it is clear that the interpolation function plays a dominant role and the dynamics at small radii do not tell anything about MOND without knowledge of the transition behavior at high accelerations (for which there is no theory). A formula which has been widely used in the case of spiral galaxies is $\mu(x) = \frac{x}{\sqrt{1+x^2}}$ (Begeman et al. 1991).

However, Famaey & Binney (2005) find that the above interpolation does not fit the Galactic rotation curve well and propose $\mu = x/(1+x)$ (but see Famaey & Binney for more detailed remarks on the shortcomings). This formula gives a smoother transition to the MOND regime, i.e. MOND effects show up earlier. These two formulas have no physical motivation other than giving satisfactory results.

Bekenstein (2004), in his relativistic TeVeS theory of gravitation, which includes the MOND phenomenology in case of small accelerations, develops for spherical symmetry the interpolation $\mu(x) = \frac{\sqrt{1+4x}-1}{\sqrt{1+4x+1}}$. This interpolation is valid only for small and intermediate accelerations and may not be valid for the full range of acceleration with which we are dealing with.

The results are shown in Fig. 18. We adopted again $M/L_R = 6.8$ (an M/L_R of 4.3 would in any case not be compatible with MOND). The dashed lines are the circular velocities derived from GCs with their anisotropies indicated. The dotted line is the Newtonian circular velocity due to the luminous component alone. The solid lines represent the MOND circular velocities with the uppermost one being the interpolation of Bekenstein, the middle one Famaey & Binney's, and the lower one the "standard" interpolation. Apparently, MOND reproduces the circular velocities derived from GC kinematics quite well within the uncertainties. The minimal conclusion is that NGC 4636 does not provide a counterargument for MOND. The shape of Bekenstein's interpolation at small radii is probably irrelevant, but also at large radii the deviation from our

mass models is quite large and becomes larger with declining M/L . The interpolation of Famaey & Binney works seemingly better than the "standard" formula, but the existent data are, however, not sufficient to perform a critical test. A case against MOND could perhaps emerge (it only can be falsified, not verified) if the suspected drop of the velocity dispersion was to be confirmed in combination with a clear tangential bias. The necessary data set must then allow also the measurement of higher moments of the velocity dispersion. NGC 4636 has already a rich cluster system, is more or less spherical, and has a relatively isolated location. Thus one may conclude that critical tests are difficult to perform with elliptical galaxies. But it is worth mentioning that so far, one of the most interesting arguments comes from X-rays. Buote et al. (2002) note that the ellipticities of the X-ray isophotes around NGC 720 at larger radii are larger than those expected from the equipotential surfaces calculated from the visible mass distributions. This holds for both the Newtonian and the MOND case.

10. Conclusions

This is the first dynamical study of the globular cluster system of the giant elliptical galaxy NGC 4636. Several hundred medium resolution spectra were acquired at the VLT with FORS 2/MXU. We obtained velocities for 174 globular clusters in the radial range $0'.90 < R < 15'.5$, or $0.5 - 9 R_c$ in units of effective radius. Assuming a distance of 15 Mpc, this corresponds to projected galactocentric distances in the range 4 to 70 kpc. Due to the sharp decrease in the GC radial number density at $7' - 9'$ about 90 per cent of our clusters are found in the range $1' < R < 7'.5$, i.e. within 4.5 effective radii. This implies that the dynamics beyond this radius cannot be determined with the current data set. Within this radius, however, we find a roughly constant velocity dispersion for the blue clusters. The red clusters are found to have a distinctly different behavior: at a radius of about $3'$, the velocity dispersion drops by $\sim 50 \text{ km s}^{-1}$ to about 170 km s^{-1} which then remains constant out to a radius of $7'$. The cause might be the steepening of the number density profile at $\sim 3'$ observed for the red clusters. Following this line of thought, one would expect a dramatic drop in the velocity dispersion for both red and blue clusters at $7' - 9'$, corresponding to the observed change in the power-law exponent of the GC number density. The observational difficulty will be to pick up sufficient clusters in this region of low surface density. In order to derive a mass profile, we perform a spherical Jeans-analysis. For a given stellar mass-to-light ratio, a model dark matter halo, and an orbital anisotropy, we calculate the projected velocity dispersion and choose those halos which minimize the residuals to the observational data. An important obstacle is the uncertain outermost data bin, which permits a large variety of halos to fit. Generally, slightly tangential models fit better than radial ones. Adopting the high stellar M/L value of Kronawitter et al. (2000) ($M/L_R=6.8$), we find within 30 kpc for $\beta = -0.5$ an M/L_R -value of 12, corresponding to a dark matter fraction of 27%. But also values as high as 26 cannot be ruled out with certainty, depending on the treatment of the last bin. When a lower stellar M/L value is used (Loewenstein et al. 2003) ($M/L_R=4.3$), the amount of dark mat-

ter that is needed to explain the observed circular velocities increases correspondingly. Massive dark matter halos (up to 76% dark matter can be required. Neither of the models can be ruled out. An important source of uncertainty is the sparse data at the outer radius. However, for most of the reasonable models, we found either less dark matter than X-ray studies with ROSAT at small radii or the halos are so concentrated that the total mass is distinctly smaller. One should consider that the claim for the very high dark matter fraction is based upon X-ray luminosities that arise in a region suspected to be out of hydrostatic equilibrium, so one must proceed with caution. The flattening of the ASCA mass profile cannot be seen. It seems that the dark matter problem in NGC 4636 also depends to a large part on the uncertain M/L value of the luminous matter. A dynamical re-investigation of the inner stellar region would therefore be worthwhile. Furthermore, it would be of great interest to obtain more spectra for globular clusters in the radial range beyond $7'$ to see whether the suspected decline in the velocity dispersion can be confirmed. To answer the question whether the NGC 4636 globular cluster systems rotates, it is desirable to obtain a more uniform angular coverage. We also investigated whether the dynamics are consistent with Modified Newtonian Dynamics and answer that positively. The difficulty is that the deep MOND regime is beyond our radial coverage. Because MOND does not predict the behavior of the circular velocity in the transition region one has to apply physically unmotivated interpolation formulae. The interpolation given by Famaey & Binney (2005) seems to work best.

Acknowledgements. We thank the referee, Michael Loewenstein, for constructive criticism which led to an improved dynamical analysis. Y.S. thanks the DAAD for supporting her stay in Concepción and acknowledges support from the Graduiertenkolleg “Galaxy Groups as Laboratories for Baryonic and Dark Matter” and a German Science Foundation Grant (DFG-Projekt HI-855/2). T.R. and B.D. acknowledge support from the Chilean Center for Astrophysics, FONDAF No.15010003.

References

- Ashman, K. M. & Zepf, S. E. 1998, *Globular cluster systems*, Cambridge astrophysics series 30, Cambridge University Press, Cambridge
- Begeman, K. G., Broeils, A. H. Sanders, R. H. 1991, *MNRAS*, 249, 523
- Bekenstein, J. D., Milgrom, M. 1984 *ApJ*, 286, 7
- Bekenstein, J. D., 2004 *Phys. Rev. D*, vol. 70, Issue 8, id. 083509
- Bell, E. F., McIntosh, D. H., Katz, N., & Weinberg, M. D. 2003, *ApJS*, 149, 289
- Bender, R., Saglia, R. P., & Gerhard, O. E. 1994, *MNRAS*, 269, 785
- Bessell, M. S., Castelli, F., & Plez, B. 1998, *A&A*, 333, 231
- Binggeli, B., Sandage, A., & Tammann, G. A. 1985, *AJ*, 90, 1681
- Binney, J. & Tremaine, S. 1987, *Galactic Dynamics*, Princeton University Press, Princeton
- Bottinelli, L. & Gouguenheim, L. 1978, *A&A*, 64, L3
- Bullock J. S., Kolatt T. S., Sigad Y. et al. 2001, *MNRAS*, 321, 559
- Buote, D. A., Jeltama, T. E., Canizares, C. R. Garmire, G. P. 2002, *ApJ*, 577, 183
- Burstein, D. & Heiles, C. 1982, *AJ*, 87, 1165
- Côté, P., McLaughlin, D. E., Hanes, D. A. et al. 2001, *ApJ*, 559, 828
- Côté, P., McLaughlin, D. E., Cohen, J. G., & Blakeslee, J. P. 2003, *ApJ*, 591, 850
- de Vaucouleurs, G., de Vaucouleurs, A., Corwin, H. G., et al. 1991, *Third Reference Catalogue of Bright Galaxies*, Springer, New York
- Dirsch, B., Richtler, T., Geisler, D. et al. 2003, *AJ*, 125, 1908
- Dirsch, B., Richtler, T., Geisler, D., et al. 2004, *AJ*, 127, 2114
- Dirsch, B., Schuberth, Y., Richtler, T. 2005, *A&A*, 433, 43
- Fall, S. M. & Zhang, Q. 2001, *ApJ*, 561, 751
- Famaey, B. and Binney, J., 2005 *MNRAS*, 363, 603
- Forman, W., Jones, C., & Tucker, W. 1985, *ApJ*, 293, 102
- Forte, J. C., Faifer, F. & Geisler, D. 2005, *MNRAS*, 357, 56
- Gerhard, O., Kronawitter, A., Saglia, R. P., & Bender, R. 2001, *AJ*, 121, 1936
- Giclas, H. L. 1939, *PASP*, 51, 166
- Hanes, D. A. 1977, *MmRAS*, 84, 45
- Harris, W. E. 1996, *AJ*, 112, 1487
- Harris, W.E., van den Bergh, S. 1981, *AJ*, 86, 1627
- Idiart, T. P., Michard, R., & de Freitas Pacheco, J. A. 2003, *A&A*, 398, 949
- Ikebe Y., Ezawa H., Fukazawa Y. et al. 1997, *Nature* 379, 427
- Jones, C., Forman, W., Vikhlinin, A., et al. 2002, *ApJ*, 567, L115
- Jones, C., Stern, C., Forman, W., et al. 1997, *ApJ*, 482, 143
- Kissler, M., Richtler, T., Held, E. V., et al. 1994, *A&A*, 287, 463
- Knapp, G. R., Faber, S. M., & Gallagher, J. S. 1978, *AJ*, 83, 11
- Krishna Kumar, C. & Thonnard, N. 1983, *AJ*, 88, 260
- Kronawitter, A., Saglia, R. P., Gerhard, O., & Bender, R. 2000, *A&AS*, 144, 53
- Kundu, A. Whitmore, B. C. 2001, *AJ*, 121, 2950
- Larsen, S. S., Brodie, J. P., Huchra, J. P. et al. 2001, *AJ*, 121, 2974
- Loewenstein, M., Mushotzky, F. 2003, *Nuclear Physics B Proc. Suppl.*, 124, 91
- Loewenstein, M., Mushotzky, R. F., Angelini, L., et al. 2001, *ApJ*, 555, L21
- Magorrian J., Ballantyne D. 2001, *MNRAS*, 322, 702
- Mamon, G. A., Łokas, E. L. 2005, *MNRAS*, 363, 705
- Matsushita, K., Makishima, K., Ikebe, Y., et al. 1998, *ApJ*, 499, L13
- Merritt, D. & Tremblay, B. 1993, *AJ*, 106, 2229
- Milgrom, M. 1983, *ApJ*, 270, 365
- Milgrom, M. 1986, *ApJ*, 302, 617
- Milgrom, M. & Sanders, R. H. 2003, *ApJ*, 599, L25
- Navarro J.F., Frenk C.S., White S.D.M. 1997, *ApJ*, 490, 493
- Ohto A., Kawano N., Fukazawa Y. 2003, *PASJ*, 55, 819
- O’Sullivan, E., Vrtilik, J. M. & Kempner, J. C., 2005, *ApJ*, 624, L77
- Paolillo M., Fabbiano G., Peres G., Kim D.-W. 2002, *ApJ*, 565, 883
- Pointecouteau, E. & Silk, J., 2005, *MNRAS*, 364, 654
- Pryor, C. & Meylan, G. 1993, in “The Structure and Dynamics of Globular Clusters”, *ASP Conf. Ser. Vol. 50*, eds. S. G. Djorgovski and G. Meylan, p. 357
- Reed, D., Governato, F., Verde, L. et al. 2005, *MNRAS* 357, 82
- Richtler, T., Dirsch, B., Gebhardt, K., et al. 2004, *AJ*, 127, 2094
- Romanowsky, A. J., Douglas, N. G., Arnaboldi, M. et al. 2003, *Science*, 301, 1696
- Sanders, R. H. & McGaugh, S. S. 2002, *ARA&A*, 40, 263
- Sanders, R. H. 2003, *MNRAS*, 342, 901
- Stephens, M. A. 1974 *Journal of the American Statistical Association*, 69, 730
- Temi, P., Mathews, W. G., Brighenti, F., & Bregman, J. D. 2003, *ApJ*, 585, L121
- Tonry, J. & Davis, M. 1979, *AJ*, 84, 1511
- Tonry, J. L., Dressler, A., Blakeslee, J. P., et al. 2001, *ApJ*, 546, 681
- van der Marel, R. P., 1994, *MNRAS*, 270, 271
- Wegner, G., Bernardi, M., Willmer, C. N. A. et al. 2004, *AJ*, 126, 2268

- Xu, H., Kahn, S. M., Peterson, J. R., et al. 2002, *ApJ*, 579, 266
Yoshii, Y., Tsujimoto, T., & Nomoto, K. 1996, *ApJ*, 462, 266
Yungelson, L., Livio, M., Tutukov, A., & Kenyon, S. J. 1995, *ApJ*,
447, 656
Zhao, H., 1997, *MNRAS*, 287, 525
Zwicky, F. 1939, *PASP*, 51, 36

The appendix lists the heliocentric velocities of globular clusters and foreground stars. The object identification follows the scheme #field.#mask #slit. The coordinates are for equinox 2000. The colors and magnitudes are from Dirsch et al. 2005. It is available in electronic form.

Appendix A: Velocities